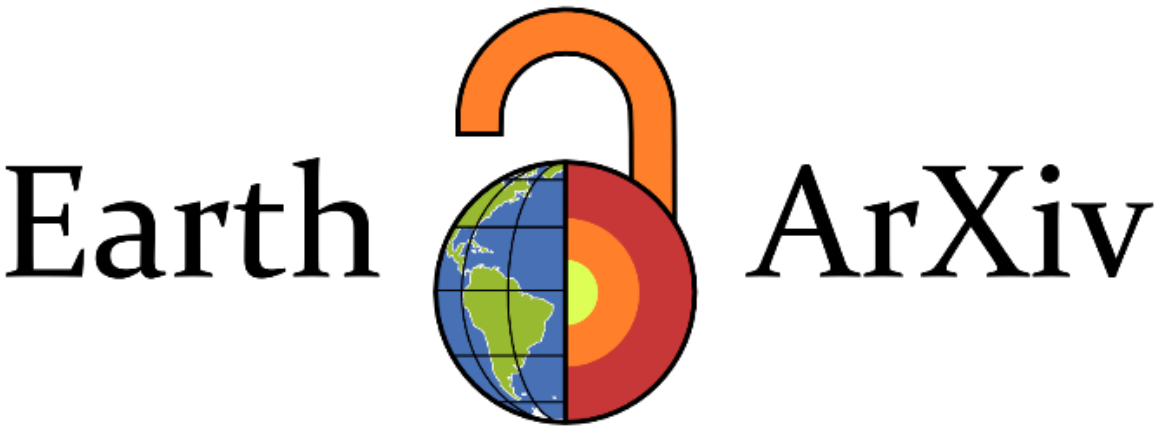


GeoPFN: subsecond geological field reconstruction with constrained uncertainty maps

Peer review status:

This is a non-peer-reviewed preprint submitted to EarthArXiv.

Journal submission. This preprint has also been submitted to *Engineering Geology* for peer review.

Authors

Sopheakpolin Mom (corresponding author)
Department of Civil and Environmental Engineering, Graduate School of Engineering, Tohoku University, 6-6-06 Aramaki Aoba, Aoba-ku, Sendai, Miyagi 980-8579, Japan
mom.sopheakpolin.p8@dc.tohoku.ac.jp

Yu Otake
Department of Civil and Environmental Engineering, Graduate School of Engineering, Tohoku University, 6-6-06 Aramaki Aoba, Aoba-ku, Sendai, Miyagi 980-8579, Japan
yu.otake.b6@tohoku.ac.jp

Stephen Wu
Research Center for Materials Informatics, Department of Advanced Data Science, The Institute of Statistical Mathematics, Research Organization of Information and Systems, 10-3 Midori-cho, Tachikawa, Tokyo 190-8562, Japan; Department of Statistical Science, The Graduate University for Advanced Studies (SOKENDAI), 10-3 Midori-cho, Tachikawa, Tokyo 190-8562, Japan
stewu@ism.ac.jp

Submitting author's ORCID: https://orcid.org/0009-0008-6532-6630

GeoPFN: subsecond geological field reconstruction with constrained uncertainty maps

Sopheakpolin Mom[a] (corresponding author), Yu Otake[a], Stephen Wu[b,c]

[a] Department of Civil and Environmental Engineering, Graduate School of Engineering, Tohoku University, 6-6-06 Aramaki Aoba, Aoba-ku, Sendai, Miyagi 980-8579, Japan

[b] Research Center for Materials Informatics, Department of Advanced Data Science, The Institute of Statistical Mathematics, Research Organization of Information and Systems, 10-3 Midori-cho, Tachikawa, Tokyo 190-8562, Japan

[c] Department of Statistical Science, The Graduate University for Advanced Studies (SOKENDAI), 10-3 Midori-cho, Tachikawa, Tokyo 190-8562, Japan

Email addresses: mom.sopheakpolin.p8@dc.tohoku.ac.jp (S. Mom); yu.otake.b6@tohoku.ac.jp (Y. Otake); stewu@ism.ac.jp (S. Wu)

Abstract

Characterising spatially variable geological fields from sparse, noisy measurements remains challenging, particularly where abrupt geological contacts occur between sensors. This study presents GeoPFN, a prior-data fitted network that reconstructs clean hydraulic conductivity and pointwise predictive uncertainty from readings on irregular sensor layouts and a supplied noise level in less than a second on a GPU. Beyond the predictive mean, GeoPFN yields two constrained uncertainty maps. The structural component responds to observations and sensor geometry and can highlight incompletely sampled contacts, channels and lenses, whereas the measurement component depends on sensor layout and the supplied noise level. Evaluated on thousands of held-out fields from a synthetic geological prior, GeoPFN attained near-nominal pooled coverage with sharp predictive intervals. In paired synthetic benchmarks, it achieved better probabilistic scores and narrower intervals than kriging at similar coverage. A smaller exploratory comparison showed lower prediction error, narrower intervals and coverage closer

to nominal than TabPFN-3.5. Sequential-sensing demonstrations showed that the maps can be updated rapidly as observations accumulate. These findings suggest that GeoPFN could support uncertainty-aware geotechnical site characterisation and automated survey updates.

Keywords: prior-data fitted networks; uncertainty quantification; probabilistic calibration; site characterisation; geotechnical engineering; hydraulic conductivity

1. Introduction

Site characterisation requires the inference of subsurface geological conditions and the spatial distribution of geotechnical properties from limited observations. Natural formations contain stratigraphic boundaries, depositional structures and discontinuities, so hydraulic conductivity K can vary by several orders of magnitude across geological contacts, channels and lenses. These variations affect seepage paths and hydraulic gradients in embankments and foundations (Cho, 2012; Liu et al., 2017). Sparse observations may be consistent with multiple geological configurations, and measurement noise can further obscure the underlying structures. Reliable site characterisation therefore requires reconstructing property fields, quantifying their predictive uncertainty and updating both efficiently as observations become available.

Random fields provide a probabilistic framework for this variability. Phoon and Kulhawy (1999) distinguished inherent variability, measurement error and transformation uncertainty, and subsequent developments established a basis for reliability-based design and uncertainty-informed decision-making (Otake and Honjo, 2022; Phoon et al., 2022a). Because natural formations are often nonstationary, trend and random components have been estimated using sparse Bayesian learning and Gaussian process regression (Ching and Phoon, 2017; Yoshida et al., 2021). More recent approaches jointly characterise stratigraphic configurations and property variability (Gong et al., 2021; Li et al., 2025; Ching et al., 2026) and use machine-learning and Bayesian methods to reconstruct geological structures and properties from incomplete borehole and cone penetration test data, including evaluations at real sites (Chen et al., 2023; Bouayach et al., 2025; Qian and Shi, 2026; Zhou et al., 2026).

Despite these advances, two challenges remain. First, most approaches require covariance func-

tions, trend assumptions or calibration procedures tailored to particular geological conditions and observation layouts. Consistent probabilistic inference for fields containing abrupt stratigraphic boundaries and localised discontinuities therefore remains difficult when the number, arrangement and precision of observations vary, and such changes usually require refitting or retraining. Second, beyond the overall magnitude of predictive uncertainty, it is important to know whether the uncertainty arises from unresolved geological structure or from the quantity, arrangement and precision of the observations. This distinction provides a basis for deciding where to investigate, how many observations to obtain and what measurement precision is required, and thus supports value-of-information analysis and exploration design (Yoshida et al., 2018; Zhao et al., 2023).

Given the scarcity of real-world geotechnical property data, conditioning on site observations alone cannot sufficiently constrain the predictive uncertainty (Wang et al., 2016; Phoon et al., 2022b; Ching et al., 2026). Prior-data fitted networks (PFNs) address this limitation and the first challenge by learning conditional prediction across tasks sampled from a prior distribution, which amortises the cost of probabilistic inference so that a new task requires a single forward pass (Müller et al., 2022; Hollmann et al., 2025). In this study, we develop GeoPFN, a PFN for rapid probabilistic reconstruction of hydraulic conductivity, a property with strong spatial heterogeneity and abrupt contrasts across geological structures. GeoPFN is trained on reconstruction tasks drawn from a synthetic geological prior containing layers, channels, lenses, faults, fractures and other structures. Given an unordered set of sensor locations, noisy readings and the supplied noise level, it predicts the clean $\log_{10} K$ field and its pointwise predictive distribution at arbitrary query coordinates without site-specific retraining.

To address the second challenge, GeoPFN represents predictive uncertainty with two architecturally constrained variance components instead of a single variance. The structural component responds to observed values and sensor geometry and is intended to highlight insufficiently resolved contacts and features. The measurement component depends on sensor geometry and the supplied noise level, with a prescribed monotonic response to noise magnitude. Because the likelihood depends only on their sum, the components do not form a uniquely identifiable physical decomposition. They nevertheless show how predictive uncertainty responds to geological information and to measurement conditions, and they provide a basis for future studies of

uncertainty reduction and observation design.

The main contributions of this study are as follows.

1. **Geological prior generator.** We develop a generator of synthetic geological fields that spans diverse classes and supports both prior-data fitting and controlled comparisons under varied observation conditions.
2. **Rapid, noise-aware field reconstruction.** In a single forward pass, GeoPFN converts irregular, noisy observations into a clean-field prediction with pointwise uncertainty, enabling the maps to be updated as new site data become available.
3. **Spatially informative uncertainty maps.** GeoPFN provides two constrained variance maps with distinct input responses. Ridges in the structural map highlight incompletely sampled contacts, channels and lenses that may merit further investigation.
4. **Systematic evaluations under matched conditions.** We examine predictive accuracy, probabilistic calibration, interval sharpness and sensitivity across geological classes, sensor densities and noise levels, comparing GeoPFN with paired kriging baselines, a single-variance ablation and TabPFN-3.5 (Jäger et al., 2026).

Sections 2–7 present related work, the model, the evaluation protocol, results, discussion and conclusions.

2. Related work and methodological position

Geological field inference. Site characterisation must account for spatial variability and measurement uncertainty (Wang et al., 2016). Coupled methods represent stratigraphy and property variability (Gong et al., 2021; Li et al., 2025), while database-informed conditional simulation generates geological and geotechnical realisations from sparse data (Ching et al., 2026). Multiple-point statistics and learned generative inversion provide further ways to encode geological structure in a prior (Strebelle, 2002; Laloy et al., 2018). GeoPFN learns a conditional predictor of pointwise log hydraulic conductivity from noisy readings and a synthetic geological prior.

Sampling and engineering decisions. Value-of-information methods guide the placement of

geotechnical observations (Yoshida et al., 2018), and information-oriented construction has used sparse site data (Otake et al., 2019). Reliability assessment then relates uncertain ground properties to an engineering response and limit state (Otake and Honjo, 2022). Rapidly updated conductivity maps may provide inputs to these workflows.

Prior-data fitted networks. Conditional neural processes predict at query points from sets of observations (Garnelo et al., 2018). PFNs learn conditional prediction across tasks sampled from a prior (Müller et al., 2022); TabPFN demonstrates this approach for tabular data (Hollmann et al., 2025), and a tabular foundation model has been applied to geotechnical site characterisation (Saito et al., 2026). GeoPFN adapts prior-data fitting to noisy spatial fields.

Predictive uncertainty. GeoPFN uses a Student-t predictive marginal related to the Normal-inverse-gamma hierarchy of deep evidential regression (Amini et al., 2020). Architectural constraints assign two variance outputs with different input responses; the predictive likelihood depends on their sum, so the split is not an identified physical decomposition (Meinert et al., 2023). Proper scores and interval coverage assess the resulting predictive distributions (Gneiting and Raftery, 2007).

Methodological position. Kriging represents spatial dependence with a covariance model (Cressie, 1993); GeoPFN learns conditional conductivity prediction across fields sampled from a geological prior. Conditional simulation generates joint field realisations, while GeoPFN returns pointwise predictive distributions and two constrained variance maps in one inference pass. TabPFN-3.5 (Jäger et al., 2026) provides a general-purpose tabular comparator; we evaluate standard and noise-aware variants. GeoPFN trains on geological fields and directly accepts the supplied noise level. Section 5.6 compares predictive accuracy, probabilistic scores, interval coverage and width, and inference time on matched synthetic observations, including a single-variance GeoPFN ablation.

3. Model formulation

3.1 Observation task

Let $Y(\mathbf{x}) = \log_{10}[K(\mathbf{x})/(1\,\mathrm{m\,s^{-1}})]$ be the clean log-conductivity field on the normalised domain $\mathbf{x} \in [0,1]^2$, where K is saturated hydraulic conductivity in m/s. The synthetic prior confines Y to $[-12, 0]$. Sensors at N locations $\mathbf{x}_i$ record

$$Z_i = Y(\mathbf{x}_i) + \varepsilon_i, \qquad \varepsilon_i \overset{\text{iid}}{\sim} \mathcal{N}(0, \sigma^2), \qquad i = 1, \ldots, N, \tag{1}$$

where the noise standard deviation σ, in $\log_{10} K$ units, is known and the same for every sensor in a field. The sensor context for one task is $D = (X, Z, \sigma)$, with $X = (\mathbf{x}_1, \ldots, \mathbf{x}_N)$ and $Z = (Z_1, \ldots, Z_N)$. At each query $\mathbf{q} \in \mathcal{Q}$, the model outputs the predictive mean of the clean field, two variance components and the degrees of freedom of its predictive distribution. The mean provides a point estimate, whereas the full distribution quantifies uncertainty about the clean value under the assumed prior and observation model.

The model accepts any query location in the domain. Training and most quantitative evaluations use the centres of a 64×64 grid (4,096 cells), with sensors sampled from those cells without replacement. Unless stated otherwise, the reported accuracy therefore refers to this grid. At $N = 4{,}096$, every cell is observed.

3.2 Architecture overview

GeoPFN maps the sensor context D and a set of query locations to the predictive mean m_q, the structural variance S_q, the measurement variance M_q and the degrees of freedom ν_q at every query (Figure 1). An observation head receives encoded locations, readings and noise level through the Transformer encoder and decoder. A geometry head receives query position, nearest-sensor distance and sensor count, but no readings or noise level. Fixed variance-split constraints transform these outputs into S_q and M_q (Table 1).

Fourier coordinate features (Tancik et al., 2020) and attention over unordered sensor sets (Lee et

Table 1. Main components of GeoPFN. For each component, the table gives its role in the network and the property that it provides to the predictions. Layer sizes and parameter counts are given in Appendix B.

Component	Role	Property
Sensor embeddings	Encode location, reading and noise level σ	Supplies information for noise-aware prediction
Sensor encoder	Self-attention among sensors, without ordering	Variable-size sensor sets with irregular layouts; order invariance
Query decoder	Cross-attention from each query to the sensors, biased to nearby ones	Predictions at arbitrary query coordinates
Observation head	Predicts the mean, structural amplitude and tail weight from encoded sensor context (Sections 3.3–3.4)	Mean and structural variance can respond to the readings
Geometry head	Predicts zero-noise measurement variance and noise-response scale from geometry alone (Section 3.3)	Measurement-variance response is independent of the readings
Variance-split constraints	Fixed formulas that assign and bound both variance components (Section 3.3)	Structural floor at sensors; measurement variance increases with σ

al., 2019) support predictions at arbitrary coordinates. The training fields contain abrupt contacts between materials and therefore provide examples of sharp geological boundaries.

A single model is trained for six sensor densities and for noise levels between 0 and 1; Section 5.2 examines additional densities and noise levels of up to 2. Sensor encodings can be reused across query sets, and the Student-t marginal provides intervals and exceedance probabilities (Section 5.6). The model comprises 5.8 million trainable parameters, and its layer specifications are given in Appendix B.

3.3 Architectural constraints on the variance split

At each query, GeoPFN divides predictive variance into $V_q = S_q + M_q$. We refer to S_q as the *structural variance*, because it responds to the readings and can highlight inferred boundaries, and to M_q as the *measurement variance*, because it responds to the sensor geometry and the noise level.

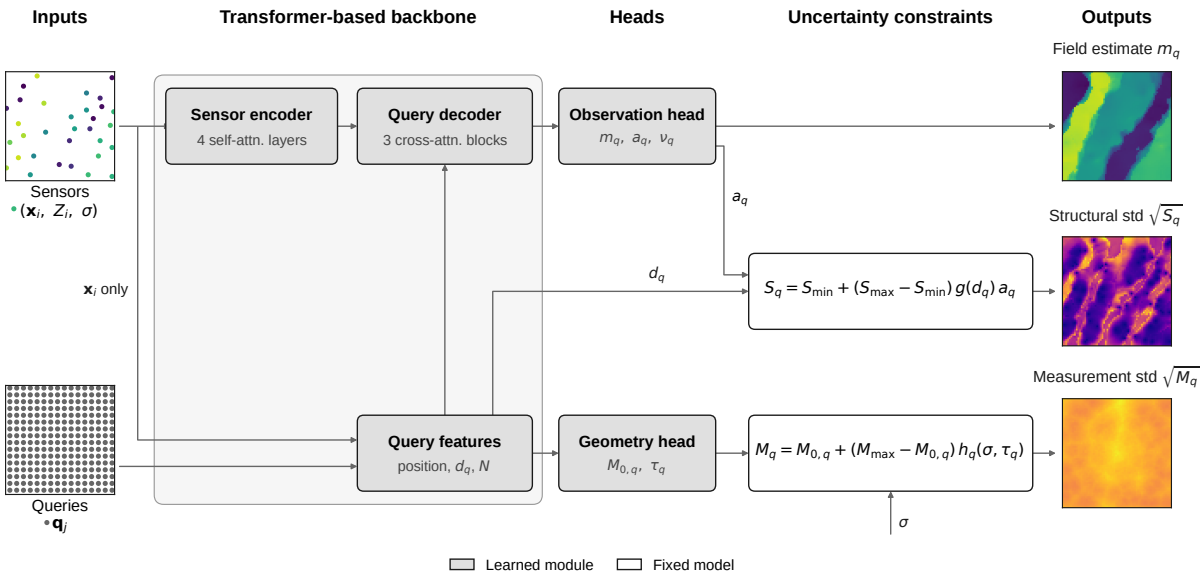


Figure 1. Architecture of GeoPFN, shown with illustrative inputs and outputs. Grey boxes denote learned modules, and white boxes denote the fixed constraints that assign the variance components. The observation head receives the sensor locations, readings and noise level through the Transformer encoder and decoder, whereas the geometry head receives only the query coordinates and the sensor geometry. The output maps show the predictive mean m_q and the structural and measurement standard deviations, $\sqrt{S_q}$ and $\sqrt{M_q}$; each map has its own colour scale. Attn., attention. The GeoPFN-V ablation is shown in Appendix Figure B.1.

Structural variance. Let $d_q = \min_i \|\mathbf{q} - \mathbf{x}_i\|$ be the distance to the nearest sensor. Then

$$S_q = S_{\min} + (S_{\max} - S_{\min})\, g(d_q)\, a_q, \qquad g(d_q) = 1 - e^{-d_q^2/\ell^2}, \tag{2}$$

where $S_{\min}$ and $S_{\max}$ bound the structural variance, $g(0) = 0$, and ℓ sets the gate's distance scale. The observation head learns $a_q \in (0, 1)$ from the sensor context. Because a_q varies with the readings, S_q can remain low in apparently homogeneous regions and rise near inferred contacts; it need not increase monotonically with distance.

Measurement variance. For the supplied noise level σ,

$$M_q(\sigma) = M_{0,q} + (M_{\max} - M_{0,q})\, h_q(\sigma, \tau_q), \qquad h_q(\sigma, \tau_q) = \frac{\sigma^2}{\sigma^2 + \tau_q^2}, \tag{3}$$

where $M_{\max}$ bounds the measurement variance. From query position, d_q and N, the geometry head learns the zero-noise variance $M_{0,q} < M_{\max}$ and response scale $\tau_q > 0$. It receives neither

the readings nor σ. Consequently, M_q increases monotonically with σ, grows approximately as σ^2 near zero and approaches $M_{\max}$ at high noise.

Bounds. We set both floors to $S_{\min} = M_{\min} = 10^{-4}$, corresponding to a standard deviation of 0.01. These floors keep both components strictly positive and prevent division by zero in the underlying NIG model (Section 3.4). We set the ceilings to $S_{\max} = M_{\max} = 18$, so that $V_q \leq 36$, the largest possible variance of a variable confined to the 12-unit $\log_{10} K$ range of the prior. Together, the floors and ceilings also bound the variance ratio used in that model. The remaining constants and transforms are given in Appendix B.1.

Irrespective of the learned weights and the sensor readings, these constraints guarantee four properties. At a sensor ($d_q = 0$), $S_q = S_{\min}$, whereas $S_q > S_{\min}$ everywhere else. For a fixed sensor layout, M_q increases with σ. Both components are bounded, so that $V_q = M_q + S_q \leq M_{\max} + S_{\max}$. Finally, M_q does not depend on the readings, and S_q depends on them only through a_q. It follows that the total variance increases with σ at sensors, where S_q is fixed, but not necessarily elsewhere.

3.4 Student-t prediction and Normal-inverse-gamma consistency

The model predicts a Student-t marginal distribution for the clean field at each query:

$$Y(\mathbf{q}) \mid D \sim t_{\nu_q}\big(m_q,\, s_q^2\big)\,, \qquad s_q^2 = \frac{\nu_q - 2}{\nu_q}(S_q + M_q), \qquad \nu_q > 2. \tag{4}$$

Here m_q is the predictive mean, s_q^2 is the Student-t scale squared, and $V_q = S_q + M_q$ is its finite variance. The heavier-than-Gaussian tails accommodate occasional large errors near unresolved contacts.

This parameterisation is mathematically consistent with the Normal-inverse-gamma (NIG) hierarchy used in deep evidential regression (Amini et al., 2020):

$$\begin{aligned} Y(\mathbf{q}) \mid \mu_q, \omega_q^2 &\sim \mathcal{N}(\mu_q, \omega_q^2), \\ \mu_q \mid \omega_q^2 &\sim \mathcal{N}(m_q, \omega_q^2/\lambda_q), \qquad \lambda_q > 0,\ \alpha_q > 1,\ \beta_q > 0. \\ \omega_q^2 &\sim \mathrm{IG}(\alpha_q, \beta_q), \end{aligned} \tag{5}$$

Set $\alpha_q = \nu_q/2$, $\lambda_q = M_q/S_q$ and $\beta_q = (\alpha_q - 1)M_q$. Integrating out μ_q and ω_q^2 then recovers the Student-t marginal of Eq. (4). The law of total variance gives

$$V_q = \mathrm{Var}[Y(\mathbf{q}) \mid D] = \underbrace{\mathbb{E}[\omega_q^2 \mid D]}_{M_q} + \underbrace{\mathrm{Var}[\mu_q \mid D]}_{S_q}. \tag{6}$$

The bounds keep λ_q finite and positive, while $M_q > 0$ and $\alpha_q > 1$ ensure $\beta_q > 0$. The latent variance ω_q^2 is a parameter in an equivalent predictive hierarchy and is distinct from the sensor-noise variance σ^2. The NIG identity does not establish the physical meaning or unique identification of either component; their prescribed input responses arise from the constraints of Section 3.3. The full conversion and the likelihood are given in Appendix B.2.

3.5 Training objective

Training data. Our prior generator produces clean $\log_{10} K$ fields from 12 classes (Figure 2); no measured fields are used. The evaluation archive contains 100,000 generated fields: 90,000 for training, 5,000 for validation and 5,000 for testing. All splits come from the same prior. A fixed subset of 32 validation fields is used for checkpoint selection, and the test fields are used only for the reported results. Training-split statistics normalise the readings, noise level and predicted mean. The generator classes and sampling ranges are specified in Appendix A; code for regenerating the archive is described under Data and code availability.

Optimisation objective. Training fields, sensor layouts and noise draws are sampled from this prior. Let $p_\theta(\cdot \mid D, \mathbf{q})$ denote the predictive density of the model with network weights θ, and let $p(\cdot \mid D, \mathbf{q})$ denote the posterior predictive density implied by the prior. The expected negative log likelihood (NLL) of the clean field satisfies

$$\mathscr{L}(\theta) = \mathbb{E}_{D,Y,\mathbf{q}}\big[-\log p_\theta(Y(\mathbf{q}) \mid D, \mathbf{q})\big] = \mathbb{E}_{D,\mathbf{q}}\big[\mathrm{KL}(p(\cdot \mid D, \mathbf{q}) \,\|\, p_\theta(\cdot \mid D, \mathbf{q}))\big] + C. \tag{7}$$

Here $\mathbf{q}$ is uniform over the query grid, and C is the expected entropy of $p(\cdot \mid D, \mathbf{q})$, which does not depend on θ. The equivalence follows the prior-data fitted network objective (Müller et al., 2022); the decomposition and the Student-t NLL are given in Appendix B.2. This NLL depends

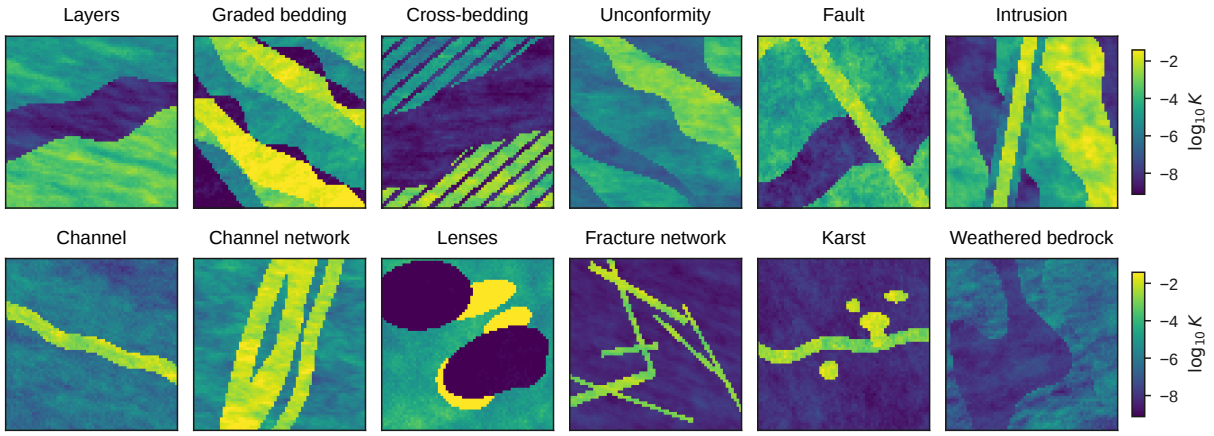


Figure 2. Synthetic geological classes used to train GeoPFN. Each panel shows one held-out example of one of the 12 classes produced by the prior generator, as a $\log_{10} K$ *field on the colour scale used in Figures 10–12 and 15. The classes range from layered and channelised sediments to faulted, fractured and karst-like settings (Appendix A). These examples are also included in the TabPFN-3.5 comparison (Table 4).*

on M_q and S_q only through $V_q = M_q + S_q$, so the likelihood alone cannot determine their split. The constraints of Eqs. (2) and (3) assign the split, and the loss contains no regulariser.

The training procedure comprises three components.

Paired noise views. Each training field has two views that share the clean target, sensor positions and a standardised Gaussian draw ξ with independent $\mathcal{N}(0,1)$ entries. View j observes $Z^{(j)} = Y(X) + \sigma^{(j)}\xi$. The first view uses a scheduled level $\sigma^{(1)} \in \{0, 0.05, 0.1, 0.2, 0.5, 1\}$; the second uses $\sigma^{(2)} \sim \mathcal{U}[0,1]$. Both are scored against the clean field. For batch size B and $|\mathcal{Q}| = 4096$ query cells, the Monte Carlo NLL estimate is

$$\hat{\mathcal{L}}(\theta) = -\frac{1}{2B|\mathcal{Q}|}\sum_{j=1}^{2}\sum_{b=1}^{B}\sum_{\mathbf{q}\in\mathcal{Q}} \log p_\theta(Y_b(\mathbf{q}) \mid X_b, Z_b^{(j)}, \sigma_b^{(j)}, \mathbf{q}). \tag{8}$$

Both views contribute to the same optimiser update, and the loss contains no pairwise consistency term.

Exhaustive schedule. The schedule crosses six sensor counts, $N \in \{4, 16, 64, 256, 1024, 4096\}$, with six noise levels, $\sigma \in \{0, 0.05, 0.1, 0.2, 0.5, 1\}$ in $\log_{10} K$ units, and uses a batch size of $B = 2$ fields per optimiser update. For each field and visit, the N sensor cells are drawn uniformly at random without replacement from the 4,096 cells of the 64×64 grid, so that $N = 4096$ senses every cell. Each of the 90,000 training fields is visited once under each of the 36 sensor-

count/noise combinations, giving $90{,}000 \times 36/B = 1{,}620{,}000$ updates. Field order is randomised independently for each combination, and updates cycle through combinations. Each field therefore appears 36 times with newly sampled sensor layouts and noise draws. This schedule retains a reproducible field archive while sampling new tasks at each update, as in PFN training (Müller et al., 2022).

Optimisation and checkpoint selection. We used AdamW with learning rate 10^{-4}, weight decay 10^{-4}, a 1,000-step warmup and cosine decay. The checkpoint with the lowest NLL on 32 fixed validation fields, at step 1,505,000, was used for all reported results. Further optimisation and numerical details are given in Appendix C.

4. Evaluation protocol

4.1 Evaluation stages

The 32 fixed validation fields were evaluated every 5,000 steps, and the checkpoint with the lowest NLL was selected (Figure 3). This checkpoint was then tested on 5,000 held-out fields across six sensor counts and eleven noise levels, with two draws per combination (66 conditions). Additional tests vary the supplied noise level and sensor count. At the maximum sensor count, every grid cell is observed and the task reduces to denoising. The full protocol is given in Appendix C.

For paired comparison, we evaluate all models on the same sensor locations and noisy measurements from 1,200 held-out fields, balanced across 12 geological classes, at six sensor counts and six scheduled noise levels (36 conditions). The comparators comprise GeoPFN-V, three kriging variants and three point-prediction models. GeoPFN, GeoPFN-V and kriging all receive the known noise level. Appendix C specifies the models and protocols. Additional tests vary sensor layout, error process and noise information (Appendices F–H). The separate 120-field TabPFN comparison is described in Section 5.6.

4.2 Metrics and uncertainty intervals

We assess point accuracy with root-mean-square error (RMSE) of the predictive mean, and probabilistic accuracy with negative log-likelihood (NLL) and continuous ranked probability score

(CRPS); lower values indicate better scores. RMSE and CRPS are reported in $\log_{10} K$ units; NLL is the negative log density on that target scale. We assess probabilistic calibration through empirical versus nominal coverage of central predictive intervals, probability integral transform (PIT) uniformity and predicted spread versus observed error. Interval width measures sharpness and must be interpreted jointly with coverage. Brier skill evaluates threshold-exceedance probabilities against a training-set climatology: positive values indicate an improvement over this reference, zero indicates equal performance and negative values indicate worse performance. For individual fields, the spread–skill ratio (SSR) compares root-mean-square predictive standard deviation with RMSE; values below one indicate under-dispersion and values above one over-dispersion (Fortin et al., 2014). Appendix C defines the metrics and their aggregation.

Confidence intervals use whole-field bootstrap resampling within geological classes, retaining all conditions for each field and keeping spatially dependent cells together (Roberts et al., 2017). We use 2,000 resamples for full-model results and 1,000 paired resamples for model differences. These intervals reflect field-sampling variability, not variation across training seeds; the full procedure is described in Appendix C.

5. Results

This section reports the inference cost, predictive quality, responses of the uncertainty components, geological examples and paired comparisons. Across the full synthetic test set, GeoPFN achieved a pooled RMSE of 1.508 $\log_{10} K$ units and 0.8975 coverage for nominal 90% intervals.

5.1 Training and inference time

Training and periodic validation required approximately 110 h on an NVIDIA RTX 6000 Ada GPU.

Training convergence. Training and validation NLL declined together (Figure 3). Over the final 220,000 steps, their mean values were 0.830 and 0.826, respectively. The selected checkpoint achieved a validation NLL of 0.8245 and a test NLL of 0.782 on 5,000 held-out fields. The close training and validation losses, together with the test result, provide evidence of generalisation to

unseen fields drawn from the same synthetic prior. Appendix C describes how the sensor-count schedule affects the training-loss curve.

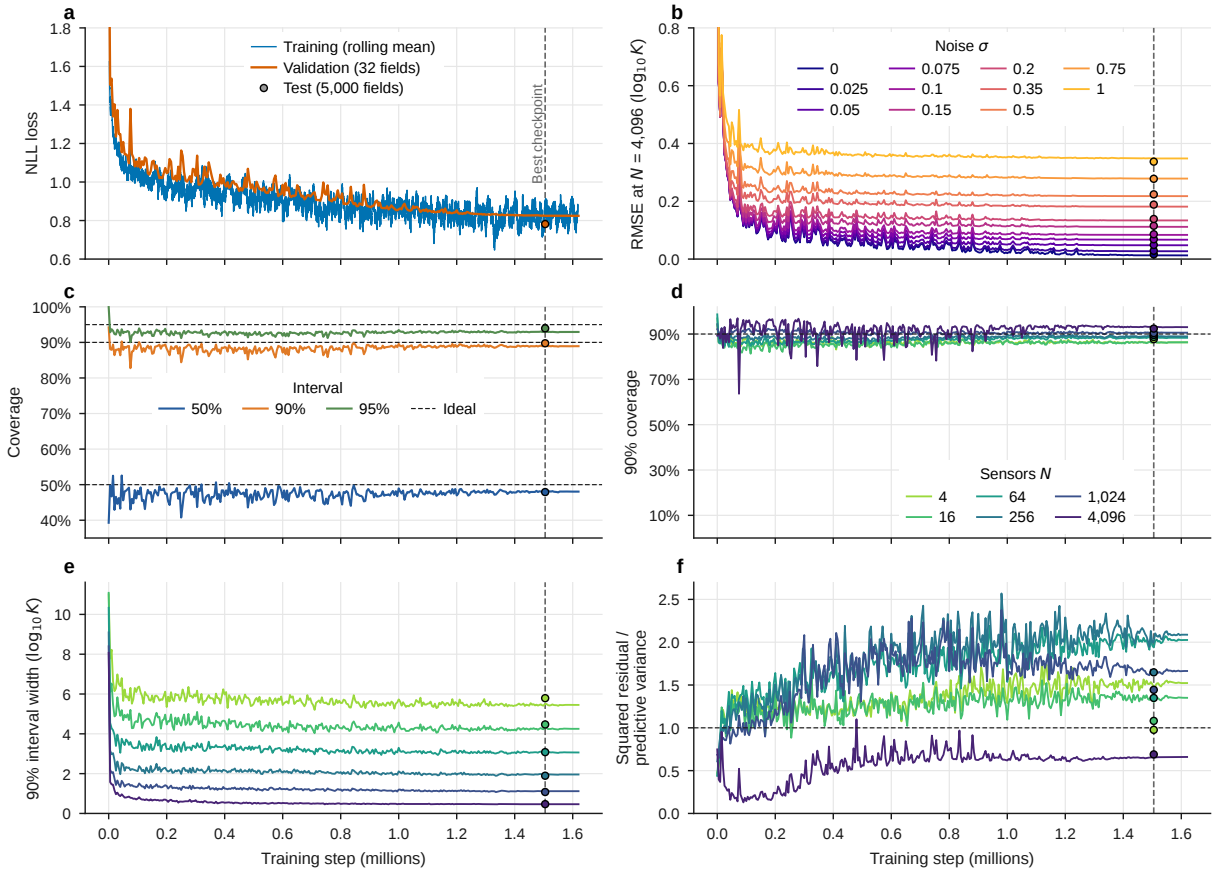


Figure 3. Training history of GeoPFN and test diagnostics of the selected checkpoint. (a) Training NLL (rolling mean), validation NLL on 32 fixed fields and test NLL on 5,000 fields. (b) Validation RMSE on the fully sensed grid, which measures denoising, for each noise level. (c) Pooled coverage of the central 50%, 90% and 95% intervals. (d–f) Test coverage of the 90% interval, mean 90% interval width and mean squared residual divided by predictive variance, for each sensor count. Dashed horizontal lines mark the ideal values, the vertical line marks the checkpoint selected by validation NLL, and circles mark its test results. The training and validation losses decline together, which is consistent with generalisation to unseen fields from the same prior.

Inference time. Table 2 reports forward-prediction latency for 4,096 query cells, including sensor encoding and all predictive outputs. Mean GPU latency was 13.4–14.0 ms for 4–1,024 sensors and 32.8 ms for 4,096 sensors; single-thread CPU latency was 135.6–4,201.9 ms. No per-field parameter fitting is required. The increase at high sensor counts is consistent with the encoder's quadratic self-attention cost.

Five warm-up calls preceded timing, and GPU calls were synchronised. Each call recomputed sensor embeddings and query features; inputs and weights remained in memory, while loading, preparation and transfers were excluded. Appendix I reports medians, variability and the full

Table 2. Mean inference time of GeoPFN per 4,096-cell field for each sensor count. Each value is the mean over 1,000 test fields (batch size one, $\sigma = 0.2$, float32, query chunks of 256 cells) and includes sensor encoding and all predictive outputs. The CPU is an Intel Xeon Platinum 8461V running one thread, and the GPU is an NVIDIA RTX 6000 Ada. GPU time is nearly constant up to 1,024 sensors and increases at 4,096 sensors, consistent with the quadratic cost of sensor self-attention.

Sensors	CPU mean (ms)	GPU mean (ms)
4	140.6	14.0
16	135.6	13.4
64	150.1	13.5
256	208.5	13.4
1,024	585.7	13.6
4,096	4,201.9	32.8

protocol. The timings in Table 2 do not constitute a comparative benchmark; a separate same-session comparison is reported in Table 4.

5.2 Accuracy and probabilistic calibration across sensor sparsity and noise

Pooled results. Across 5,000 test fields and 66 conditions, pooled RMSE was 1.508 $\log_{10} K$ units (95% field-bootstrap interval 1.498–1.519), and mean NLL was 0.782 (0.776–0.787). Mean 90% interval coverage was 0.8975 (0.8968–0.8983), close to nominal in aggregate. Pooled over noise levels, RMSE fell from 2.201 with 4 sensors to 0.886 with 1,024 sensors and 0.172 with every cell observed (Figure 4). Coverage ranged from 0.877 to 0.904 across incomplete sensor layouts; on the fully observed grid, intervals were conservative (0.924). Across individual conditions, coverage ranged from 0.852 to 0.996. All three conditions that deviated from 0.90 by more than five percentage points had $N = 4096$. Architecture checks found no violations of the structural floor or measurement-variance monotonicity; the maximum numerical error of the floor at sensor cells was 2.5×10^{-12}.

Calibration was weaker at material contacts. Across the 5,000-field test set, nominal 90% intervals covered 77.9% of boundary cells, compared with 92.0% of interior cells (Figure 5; Appendix E); these aggregates include sensed cells and fully sensed grids. In the paired benchmark excluding fully sensed grids, coverage was 74.4% at unsensed boundary cells and 91.8% at unsensed interior cells (Appendix E.1, Table E.1).

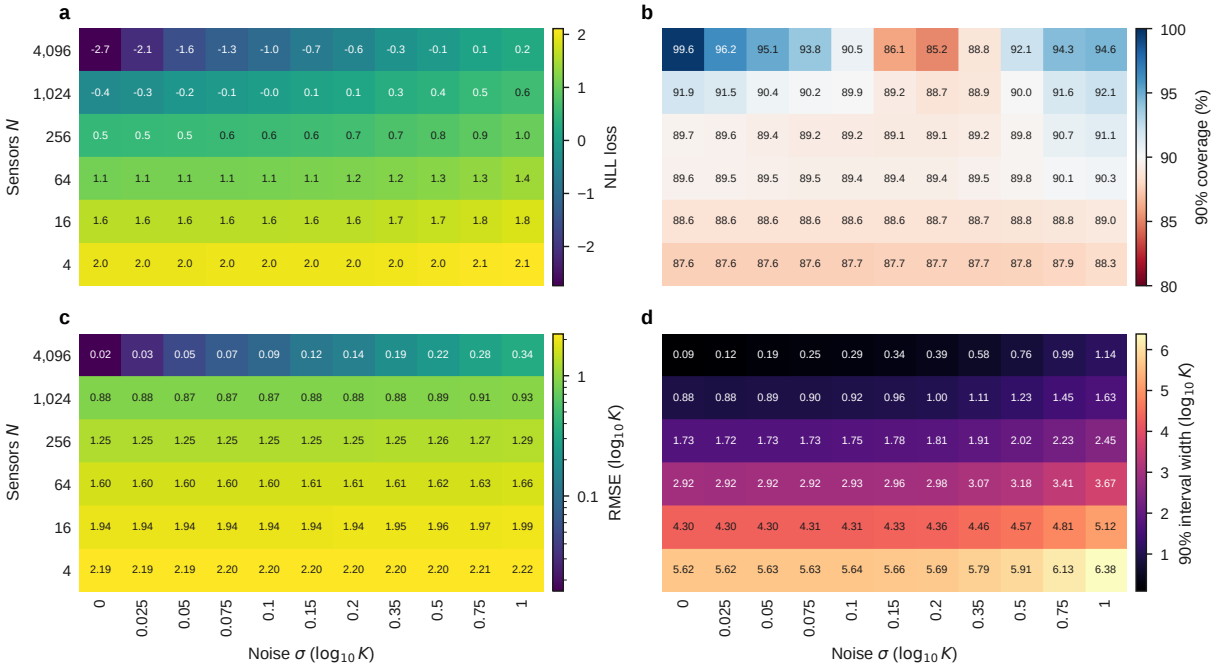


Figure 4. Performance of GeoPFN across sensor counts and noise levels on the 5,000 test fields. The panels show (a) NLL, (b) 90% interval coverage, (c) RMSE and (d) mean 90% interval width in $\log_{10} K$*. Rows correspond to sensor counts, with the densest layout at the top, and columns correspond to noise levels, with noise-free readings on the left. Errors and interval widths decrease as sensors are added, while coverage stays close to 0.90 except in some fully sensed conditions.*

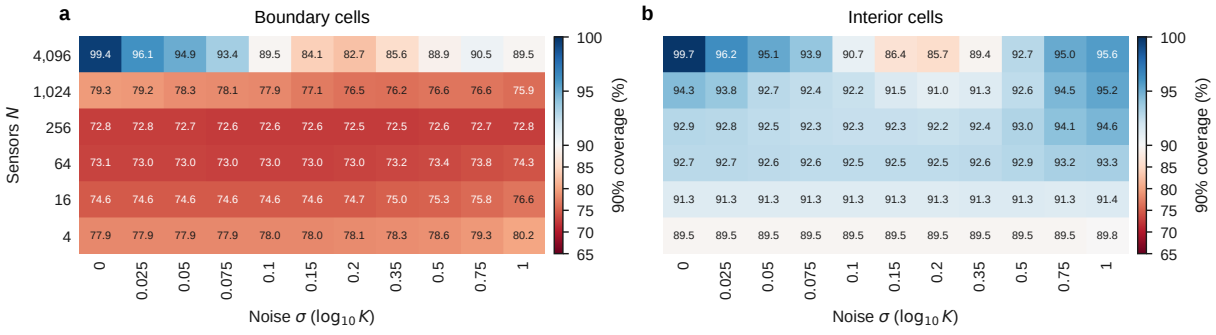


Figure 5. Coverage of nominal 90% intervals, in percent, at (a) material boundaries and (b) interior cells on the 5,000 test fields. Each cell of the heat maps pools two noise draws for one combination of sensor count and noise level. Boundary coverage remains below the nominal 90% at every sensor count short of full sensing, whereas interior cells are covered at close to the nominal rate.

At nominal 50% and 95% levels, pooled coverage was 0.479 and 0.939, respectively (Figure 6). The 95% field-bootstrap interval for 90% coverage (0.8968–0.8983) excludes the nominal value, indicating slight but detectable pooled undercoverage. Observed RMSE tracked predicted standard deviation from approximately 0.1 to 4 $\log_{10} K$; in the lowest-spread bin, which was dominated by sensor cells, observed errors were smaller than predicted. These pooled diagnostics do not offset the substantial undercoverage at unsensed boundaries. Appendix J reports additional failure cases and condition-level results.

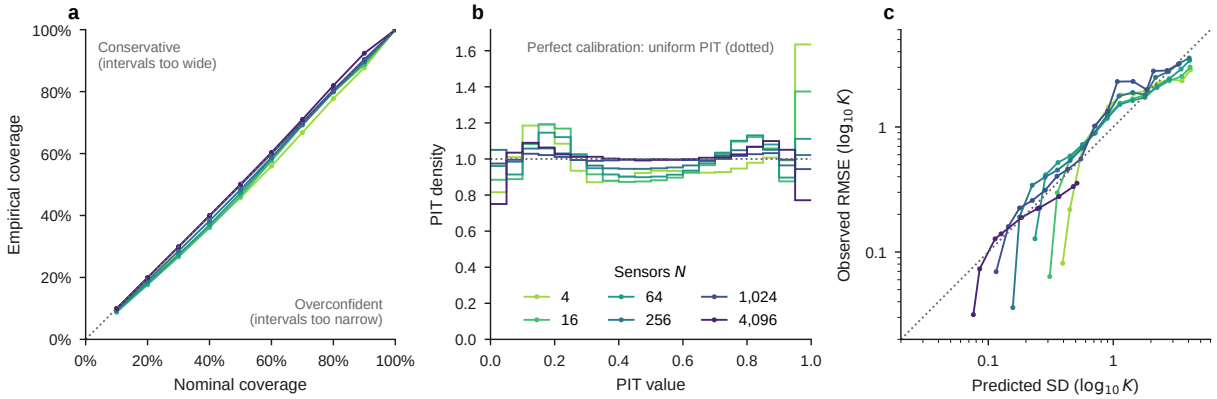


Figure 6. Probabilistic calibration of GeoPFN on the 5,000 test fields, shown separately for each sensor count. (a) Empirical coverage of central prediction intervals against their nominal level. (b) Density of the probability integral transform (PIT), which is uniform for a calibrated model. (c) Observed RMSE against predicted standard deviation, with cells binned by predicted spread. Dotted lines indicate ideal probabilistic calibration; in (b), a uniform PIT density equals one. Curves close to these lines indicate that the predicted uncertainty matches the realised error.

Distance to the nearest sensor. Figure 7 resolves scores by distance to the nearest sensor. Coverage of the 90% interval was 0.92–0.96 at sensor cells, 0.88–0.89 in the adjacent band and generally 0.87–0.92 farther away. Predicted standard deviation tracked RMSE across distance bands, while the structural standard deviation rose from its floor of 0.01 at sensors to about 1–2.4 beyond six cells.

Sensitivity to misspecified noise and untrained settings. Because σ is an input, calibration depends on the value supplied at inference. With 16 or 256 sensors, 90% coverage was 0.832–0.897 across supplied ratios $\hat{\sigma}/\sigma$ from 0 to 2 for nonzero true noise levels (Figure 8a). Sensitivity was greater on the fully observed grid: at true $\sigma = 0.5$, coverage was 0.921 with the correct input, 0.075 with $\hat{\sigma} = 0$ and 0.709 with $\hat{\sigma} = 2\sigma$. Dense sensor sets therefore require an accurate noise estimate; Appendix H evaluates two estimation methods. At true $\sigma = 1.5$ or 2, beyond the

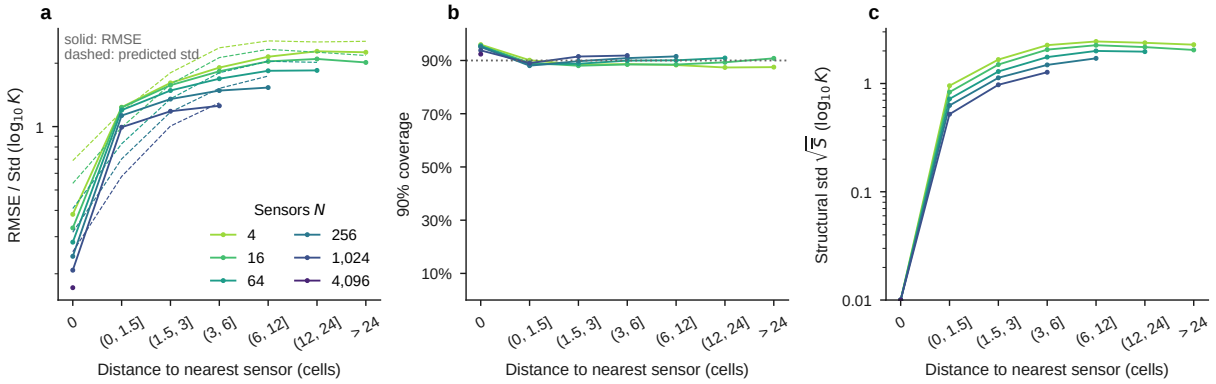


Figure 7. Accuracy and uncertainty of GeoPFN as functions of the distance to the nearest sensor, pooled over noise levels on the 5,000 test fields. (a) RMSE (solid) and root-mean predictive standard deviation $\sqrt{\bar{V}}$ (dashed); (b) 90% interval coverage; (c) root-mean structural standard deviation $\sqrt{\bar{S}}$. Overbars denote means over the cells in each distance band, and bands with fewer than 10,000 cells are omitted. At $N = 4{,}096$ every cell is a sensor, so only the sensor band exists. The predicted spread follows the error as the distance increases, and the structural standard deviation rises from its floor at the sensors.

trained range, coverage was 0.891–0.933 across the six trained sparsity levels (Figure 8b). At five untrained sparsity levels, RMSE fell between values at neighbouring trained counts (Figure 8c); coverage was 0.883–0.915 except at $N = 2048$ with $\sigma = 0$ and 1 (0.952 and 0.930). These tests alter only the inference inputs and use the same synthetic prior as training.

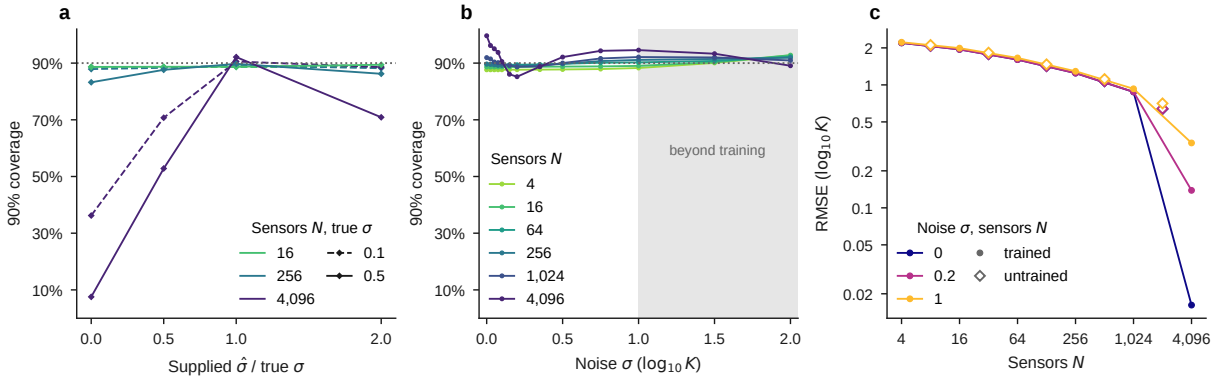


Figure 8. Sensitivity of GeoPFN to its inference inputs on the 5,000 test fields. (a) 90% coverage when the supplied noise level $\hat{\sigma}$ differs from the true level σ. (b) 90% coverage for true noise levels that include $\sigma = 1.5$ and 2, beyond the training range (shaded). (c) RMSE at the trained sensor counts (lines) and at untrained counts (diamonds). Dotted lines mark the nominal 90%. Coverage is insensitive to the supplied noise level at sparse sensor counts but depends strongly on it when every cell is sensed.

5.3 Uncertainty-map responses to sensor noise and sparsity

Overall test-set response. Across 5,000 test fields, the measurement standard deviation increased monotonically with σ at every sensor count (Figure 9): from 0.07 to 0.49 on the fully sensed

grid and from 0.80 to 1.20 with 4 sensors, and it decreased as the sensor count increased. The structural standard deviation also depended on sensor count but changed by less than 0.15 between $\sigma = 0$ and 1 at every count; it stayed at its floor of 0.01 on the fully sensed grid. RMSE changed little with σ for $N \leq 1024$, where interpolation error dominated, but rose from 0.016 to 0.34 on the fully sensed grid, where measurement noise dominated.

The decrease of the measurement standard deviation with sensor count is learned, not imposed: the constraints fix only its monotone increase with σ, whereas $M_{0,q}$ and τ_q depend on N and d_q through the geometry head. Two effects are consistent with the observed trend. First, the target is the clean field, so the noise that remains in the predictive mean decreases as more readings inform each query. Between $\sigma = 0$ and 1, the pooled measurement variance increased by 0.81 with 4 sensors, of the same order as $\sigma^2 = 1$, and by 0.23 on the fully sensed grid, where the mean averages neighbouring readings. With 4 sensors, however, the structural variance decreased by 0.68 over the same range, so that the total predictive variance increased by only 0.13, close to the realised increase in mean squared error (0.13); the model therefore reallocated part of the variance between the components rather than adding it. Second, the zero-noise standard deviation, 0.80 with 4 sensors and 0.07 on the fully sensed grid, is not caused by measurement noise. Because the likelihood constrains only the total variance, the geometry head can assign part of the sparsity-dependent interpolation error to $M_{0,q}$. At low noise, the measurement map therefore partly reflects sensor geometry rather than measurement error alone.

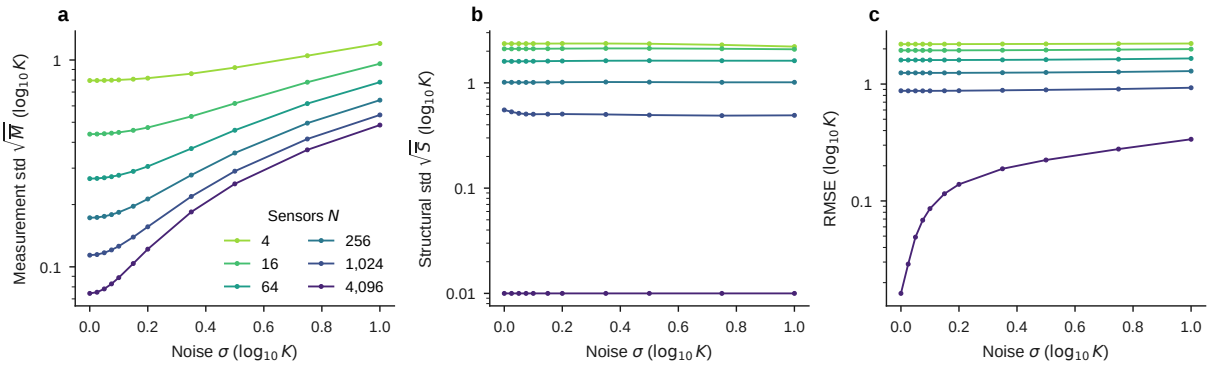


Figure 9. Average response of the two variance components to sensor count and noise level on the 5,000 test fields. (a) Root-mean measurement standard deviation $\sqrt{\overline{M}}$, (b) root-mean structural standard deviation $\sqrt{\overline{S}}$ and (c) RMSE, each plotted against the noise level for every sensor count. Overbars denote means over fields and cells. The measurement component increases with the noise level at every sensor count, whereas the structural component changes little with noise and mainly reflects sensor density.

These responses confirm the intended input dependencies; calibration itself is assessed by the distributional scores and coverage.

Response to noise level. Figures 10 and 11 vary one input at a time on a graded-bedding test field with oblique contacts. In Figure 10, every cell is sensed while σ varies over the six training levels. Structural standard deviation stays at 0.01 everywhere. Measurement standard deviation does not decrease at any cell as σ rises; its spatial mean increases from 0.074 at $\sigma = 0$ to 0.484 at $\sigma = 1$. Predictive-mean RMSE rises from 0.013 to 0.357 over the same range, so the measurement map broadly tracks residual error on this field. At $\sigma = 1$, the mean reduces the error of raw readings by a factor of about 2.8. The measurement map remains smooth rather than following contacts because the geometry head receives no readings.

Response to sensor sparsity. Figure 11 varies sensor count with noise-free readings ($\sigma = 0$). With 4 or 16 sensors, the predictive mean approaches a smooth background (RMSE 2.549 and 2.271), and structural standard deviation is high across both contacts and interiors. Its mean is higher with 16 than with 4 sensors (2.62 versus 1.79), so the response is not monotone at the sparsest layouts. From 64 sensors onward, structural standard deviation concentrates along contacts: its mean on contact cells exceeds that on interior cells by factors of 1.2, 1.9 and 1.8 at 64, 256 and 1,024 sensors, respectively. The distance gate contains no boundary information, so this localisation comes from the reading-dependent amplitude a_q. With every cell sensed, structural standard deviation reaches its 0.01 floor, and the mean reproduces clean readings (RMSE 0.013). Mean measurement standard deviation also falls, from 0.644 with 4 sensors to 0.074 with 4,096, as its geometry inputs change. These figures illustrate the prescribed input responses rather than separately identified physical sources of uncertainty.

5.4 Reconstructing geological contacts and features

Reconstruction from a regular sensor grid. Figure 12 shows six contrasting test fields: dipping layers, a buried channel, low-contrast lenses, a fault zone, a channel network and weathered bedrock. Each field uses the same 256 sensor locations on a regular 16×16 grid ($\sigma = 0.3$). The predictive means recovered the main layer contacts, channel, fault zone and the branches of the channel network, but smoothed within-material variation and the narrow connections between

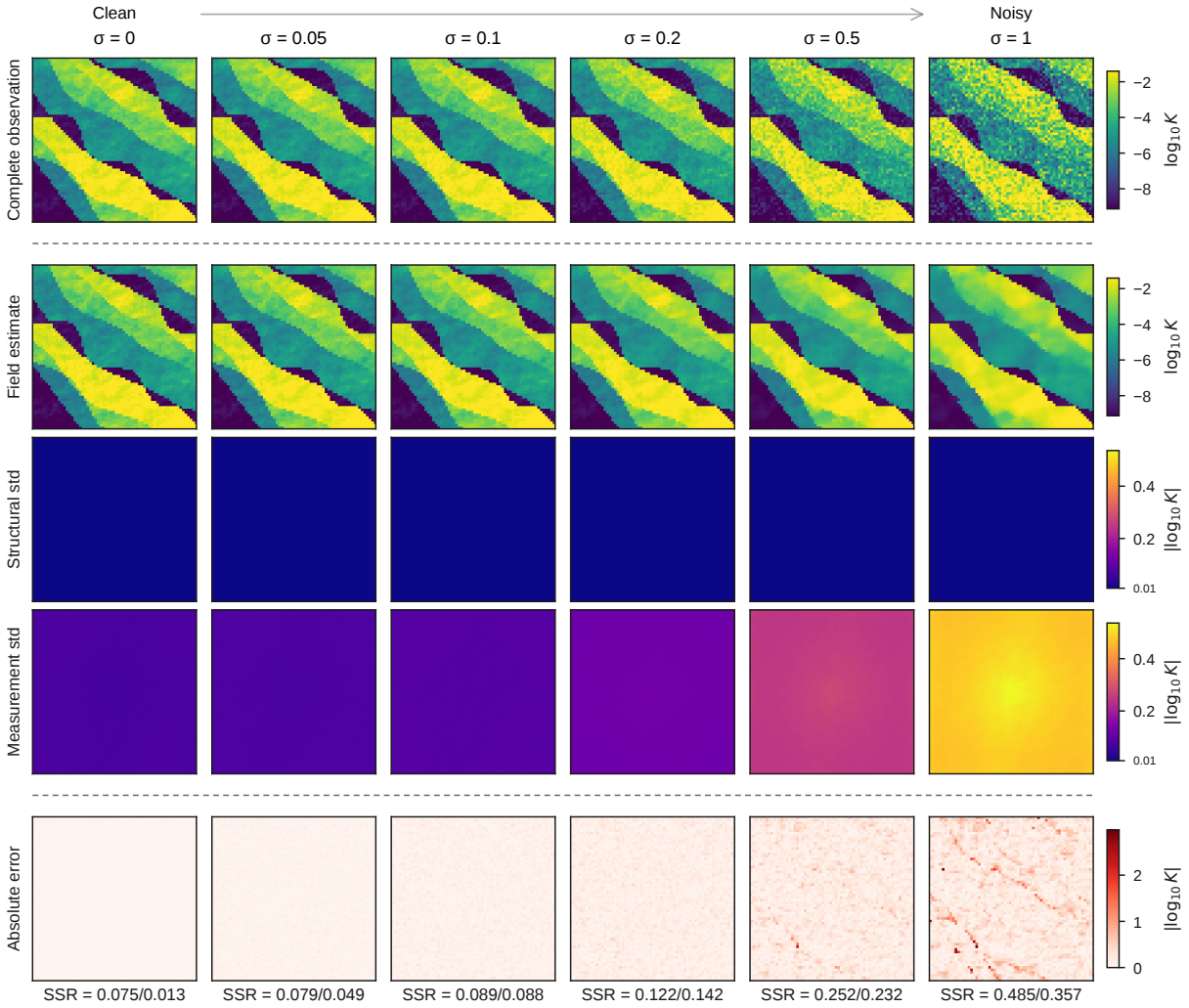


Figure 10. Response of the variance components to the noise level on a graded-bedding test field in which all 4,096 cells are sensed. Columns correspond to the six training noise levels, all using the same standardised noise draw scaled by σ. The rows show the ground truth and the noisy observations, the model outputs (predictive mean and structural and measurement standard deviations) and the absolute error. Because every cell is sensed, the structural standard deviation stays at its 0.01 floor, while the measurement standard deviation increases with σ and broadly tracks the resulting prediction error. SSR, spread–skill ratio.

channel branches. Field RMSE ranged from 0.434 for lenses and weathered bedrock to 0.950 for the channel network.

Structural standard deviation formed ridges along several reconstructed contacts and around the channel and lenses, despite lens–background contrasts of at most 1.73 $\log_{10} K$. It reached its floor at sensors and remained low along the low-contrast weathering front. We used $\sigma = 0.3$ because $\log_{10} 2 \approx 0.30$: one noise standard deviation corresponds to a factor of two in K. Because these fields were chosen for illustration, interval calibration is assessed by the aggregate tests rather than by these examples.

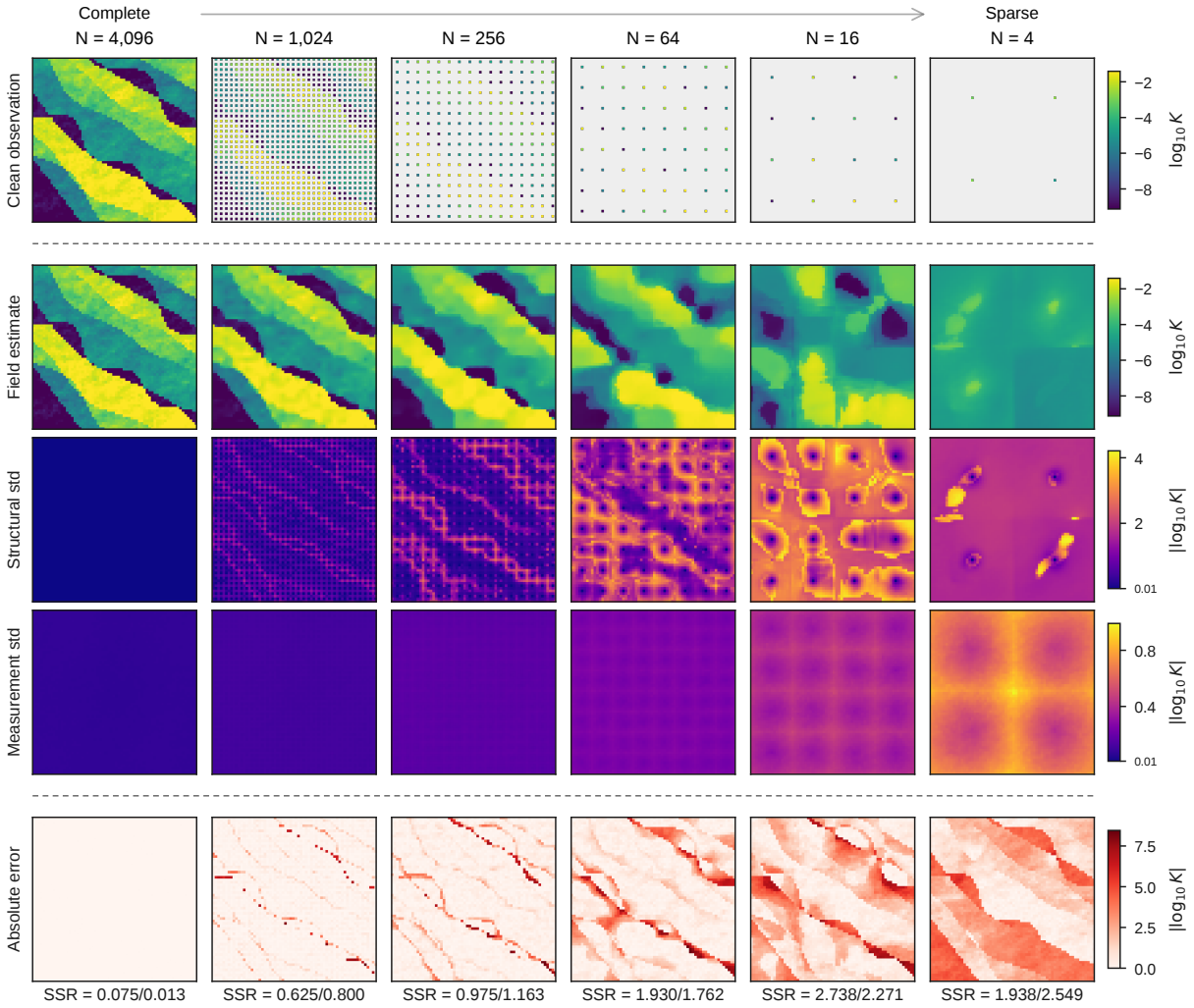


Figure 11. Response of the variance components to sensor sparsity on the same field as Figure 10, with noise-free readings ($\sigma = 0$). Columns range from all 4,096 cells sensed to only 4 sensors, and the rows are arranged as in Figure 10. The structural standard deviation stays at its 0.01 floor when every cell is sensed, concentrates near contacts at 256–1,024 sensors and is elevated across the whole field at 4–16 sensors. The measurement standard deviation also changes with sensor geometry, even though the readings are noise-free. SSR, spread–skill ratio.

Illustrative uncertainty-guided sensor placement. We applied a greedy policy to the six Figure 12 fields ($\sigma = 0.3$). Beginning with four sensors at quadrant centres, we repeatedly selected the unsensed cell with the highest structural standard deviation at least four grid cells from existing sensors, added its noisy reading from the same draw and updated GeoPFN. We capped the sequence at 64 sensors to emulate sparse field measurements. Structural standard deviation was used because the measurement map was nearly uniform within each field at fixed σ; the separation rule discouraged repeated sampling along one contact. Neither retraining nor covariance fitting was required. Each of the 60 updates required one forward pass; at up to 64 sensors, a pass took about 14 ms on a GPU or 150 ms on one CPU thread (Table 2). The 64-sensor

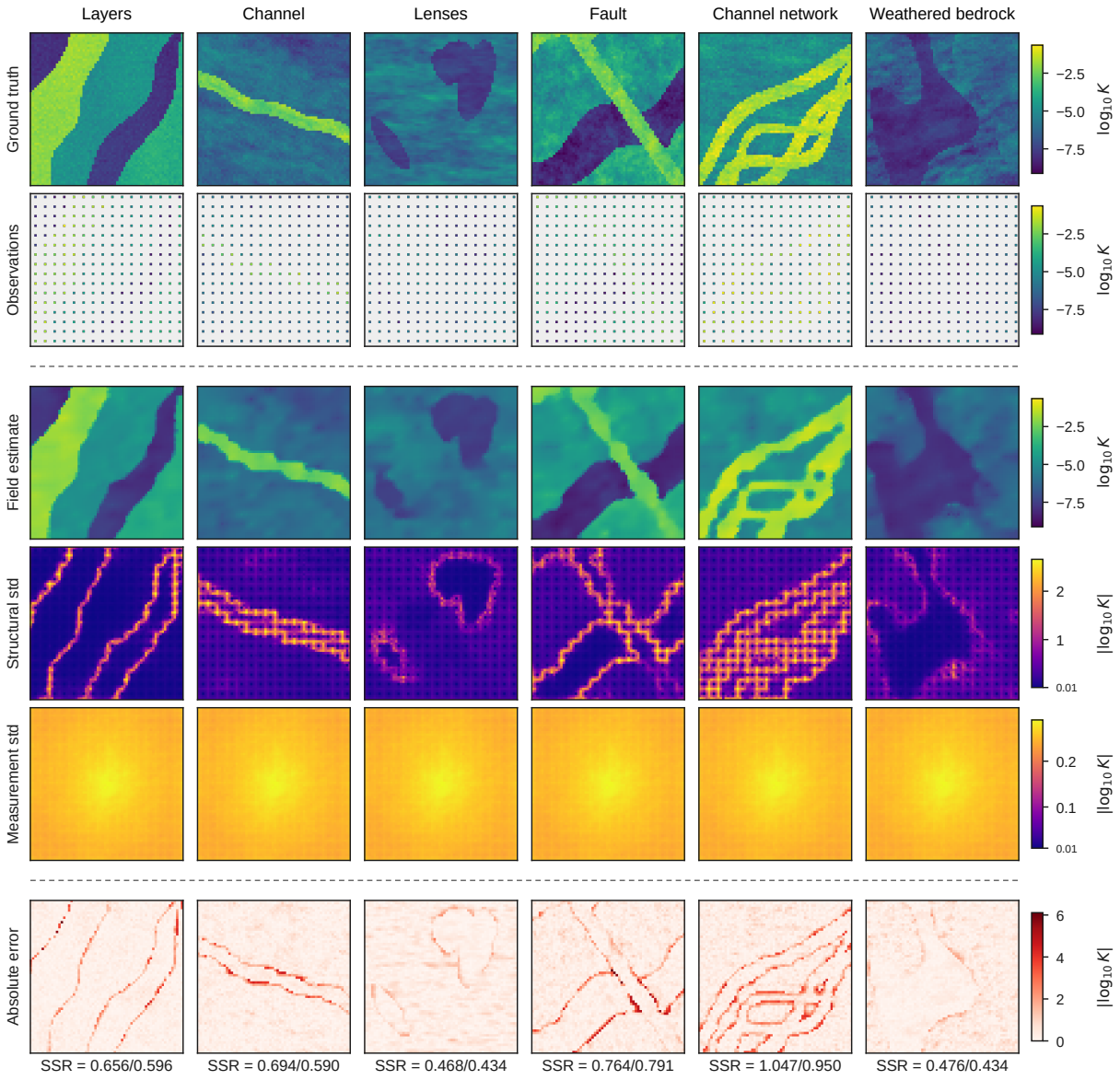


Figure 12. Reconstruction of six held-out fields with contrasting geological structure. Each field is observed at the same 256 locations on a regular 16×16 *grid with noise level* $\sigma = 0.3$. *The rows show the clean field, the observations, the predictive mean, the structural and measurement standard deviations and the absolute error. The measurement maps are identical across fields because the sensor geometry and the supplied noise level are the same. The fields were chosen for their structure, not for their reconstruction error (Appendix E.3). SSR, spread–skill ratio.*

sequential placement therefore required less than 1 s of GPU time in total, excluding acquisition and input preparation. Supplementary Video 1 animates this procedure up to 256 sensors, and Supplementary Video 2 shows a continuous sensing path that moves step by step towards the highest structural standard deviation; in both, sensors gather along unresolved contacts, channel margins and lens boundaries. The videos are illustrations, not evaluations of a sensing strategy.

The sequential reconstructions retained the main layer contacts, channel, fault zone and weathering front. The smaller lens remained faint, and branches of the channel network merged into one body; the channel-network field had the largest RMSE (1.398; Figure 13). Although σ was fixed, the selected sensor locations differed across fields, producing distinct layouts and measurement maps. Together, these examples show that GeoPFN updates field predictions rapidly as observations accumulate on irregular sensor layouts.

5.5 Unseen synthetic patterns and finer query grids

Figure 14 combines synthetic spatial forms absent from the training classes with a numerical target rescaling and a finer query grid. The six forms are a uniform field, an anisotropic random field, a thin seam, a diapir (an elliptical cap on a narrow stem), a chevron fold with straight limbs and sharp hinges, and scattered elliptical inclusions. These fields are synthetic shape analogues, not measured soil units.

The field values were mapped affinely to the Soil Behaviour Type Index range $I_c = 1.2$–3.8. This is a numerical rescaling of synthetic fields, not independent I_c data or a physical conversion from conductivity to I_c. The unchanged conductivity checkpoint received the noise-free block means as $z = -I_c$, and we display its negated predictive mean $-m_q$. Neither retraining nor recalibration was performed.

The fields were generated at 256×256 cell centres. A shared regular 16×16 sensor grid provided 256 readings, each the mean of a 4×4 fine-cell block. The model was queried at all 65,536 fine-grid centres. RMSE was 0.025 and 0.082 I_c units for the uniform and anisotropic fields, 0.330 for the thin seam and 0.305 for the diapir. The chevron fold (0.741) had missed or displaced limbs and hinges; the inclusions (0.637) were sometimes omitted or merged. Structural-standard-deviation

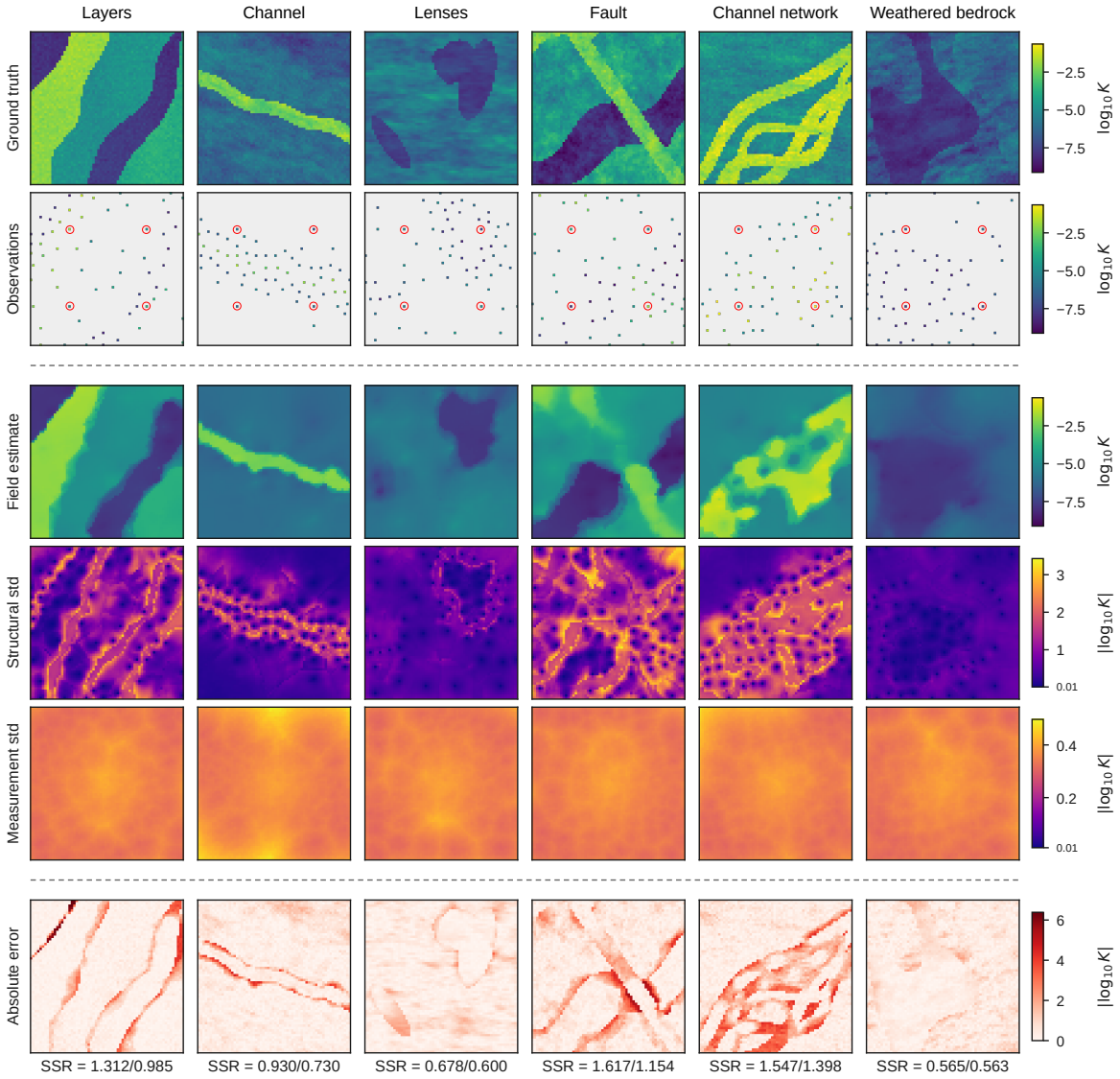


Figure 13. Uncertainty-guided sequential sensor placement on the six fields of Figure 12 ($\sigma = 0.3$). Placement starts from four sensors at the quadrant centres (red circles); each of the following 60 sensors is placed at the cell with the highest structural standard deviation among cells at least four grid cells from every existing sensor. The rows are arranged as in Figure 12, and the RMSE of each final reconstruction is printed below its field. Each layout is selected independently for its field. The example illustrates rapid prediction updates as observations accumulate on irregular sensor layouts.

ridges followed several reconstructed interfaces, while measurement maps were identical across fields because the sensor geometry and supplied noise were fixed. Median single-thread CPU forward time was 2,764.9 ms per field, excluding loading, preparation and plotting.

This illustrative test shows reconstruction of several unseen synthetic shapes at finer query resolution, but it changes structure, target scale and resolution together. It does not establish transfer to measured I_c data or calibration of uncertainty on the rescaled target. Finer queries also cannot recover structure unresolved by the sensors.

5.6 Comparison with a matched ablation and baseline models

For the 1,200-field paired benchmark, all methods used the same sensor locations, noisy readings and clean targets. GeoPFN-V is the matched single-variance ablation. Other comparators were three kriging variants with globally fitted, class-specific (oracle) or per-field restricted maximum likelihood (REML) covariance parameters (Cressie, 1993; Patterson and Thompson, 1971), and three point interpolators: inverse-distance, nearest-neighbour and natural-neighbour (Shepard, 1968; Park et al., 2006). GeoPFN, GeoPFN-V and kriging received the known noise level. The full protocols are given in Appendix C.2.

Both GeoPFN variants had lower pooled CRPS and NLL than the kriging baselines and lower RMSE than all point predictors (Table 3). GeoPFN-V had marginally lower RMSE, CRPS and NLL than GeoPFN (1.491, 0.588 and 0.755 versus 1.499, 0.591 and 0.768). GeoPFN had coverage closer to nominal (0.900 versus 0.895) and slightly narrower intervals (2.81 versus 2.84). The variance split therefore provides two diagnostic maps with little change in pooled predictive performance, without improving the scores. Compared with per-field REML kriging, GeoPFN reduced CRPS by 13% (0.591 versus 0.677) and mean 90% interval width by 28% (2.81 versus 3.92), with similar coverage (0.900 versus 0.899). The pooled RMSE advantage does not hold at every sensor count: per-field kriging had lower RMSE at 64–1,024 sensors, whereas GeoPFN retained lower CRPS. The full condition-level results are reported in Appendix D.

GeoPFN had lower CRPS than each kriging variant in all 12 generator classes; class-level CRPS differed from GeoPFN-V by at most 0.014. The largest gains over kriging occurred with 4 or

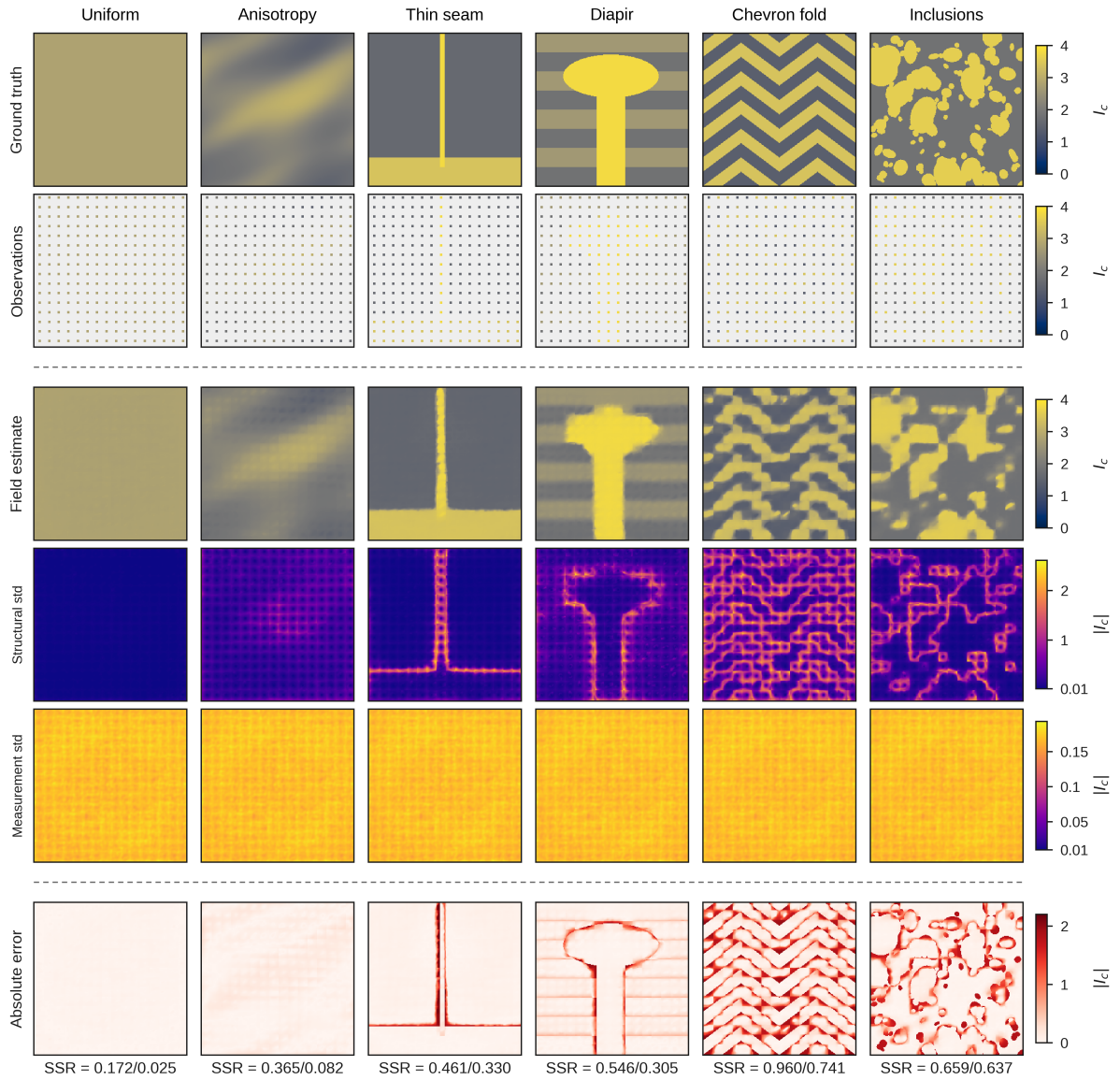


Figure 14. Reconstruction of six unseen synthetic patterns at 256×256 *resolution after numerical rescaling of the target to the soil behaviour type index* I_c*. In every field, the model receives 256 noise-free block means on the same* 16×16 *sensor grid, encoded as* $z = -I_c$*, and the displayed estimate is* $-m_q$*. The rows show the ground truth, the observations, the estimated field, the structural and measurement standard deviations and the absolute error. The variance maps were not calibrated on* I_c*. SSR, spread–skill ratio.*

Table 3. Pooled scores on the 1,200-field paired benchmark. Scores are pooled over 36 conditions (six sensor counts × six noise levels), and all models use the same fields, sensor layouts and noise draws. RMSE, CRPS and interval width are in $\log_{10} K$*. Bold marks the best value in each column; for coverage, it marks the value closest to the nominal 0.90. Point predictors provide no predictive distribution, so their probabilistic scores are not available (–). Results by sensor count are given in Appendix D.*

Model	RMSE ↓	CRPS ↓	NLL ↓	Cov. 90	Width 90 ↓
GeoPFN (this study)	1.499	0.591	0.768	**0.900**	**2.81**
GeoPFN-V	**1.491**	**0.588**	**0.755**	0.895	2.84
Kriging, global prior	1.529	0.710	1.214	0.905	4.29
Kriging, class prior (oracle)	1.519	0.693	1.147	0.898	4.09
Kriging, per-field REML	1.509	0.677	1.172	0.899	3.92
Inverse-distance weighting	1.628	–	–	–	–
Nearest neighbour	1.917	–	–	–	–
Natural neighbour	1.670	–	–	–	–

16 sensors. At 64–1,024 sensors, per-field kriging had slightly lower RMSE, although GeoPFN retained lower CRPS. With all cells observed, GeoPFN had lower denoising RMSE than per-field kriging (0.179 versus 0.297). These class and sensor-count comparisons remain within the same synthetic generator (Appendices D–E).

Where the two variance parameterisations differ. GeoPFN-V covered more unsensed contact cells (0.774 versus 0.744 for nominal 90% intervals), but its coverage fell further when the observations departed from the training conditions. With 64 sensors on survey lines, coverage was 0.827 for GeoPFN-V and 0.858 for GeoPFN; with 256 sensors in four clusters it was 0.816 and 0.842. GeoPFN also had lower CRPS than GeoPFN-V for every survey-line layout up to 256 sensors and for all cluster and half-domain layouts. Under 10-cell spatially correlated sensor errors with 4,096 sensors, coverage was 0.246 for GeoPFN-V and 0.341 for GeoPFN (Appendices F–G). Both models undercovered severely in these conditions, and each was trained with one seed, so these differences indicate a tendency rather than a general advantage of the constrained split across changed observation conditions.

Threshold-exceedance forecasts. For exceedance of the 10th, 50th and 90th percentiles of clean training values, GeoPFN achieved Brier skills of 0.621, 0.548 and 0.482 against training climatology. GeoPFN-V was marginally higher at each threshold (0.623, 0.550 and 0.483); both neural models outperformed the kriging variants (Appendix D).

Additional TabPFN comparison. We evaluated the pretrained TabPFN-3.5 regressor (Jäger et al., 2026) on 120 held-out fields (10 per class) under the same 36 conditions; every model in Table 4 and Figure 15 used identical fields, sensor layouts and noise draws. This is an exploratory comparison between a geological-prior-trained predictor and a general-purpose pretrained tabular regressor; the models use different training priors. Standard TabPFN-3.5 receives no noise input. Because its preprocessing removes task-constant columns, the noise-aware variant encodes σ in two coordinate-derived features rather than as a constant column (Appendix C.2).

GeoPFN had lower RMSE and CRPS than both TabPFN variants (Table 4). In the local timing comparison, GeoPFN required 17 ms per field, versus 730 and 750 ms for standard and noise-aware TabPFN-3.5, respectively; TabPFN times include fitting and prediction under its default mixed precision. The timed spans have different input/output conventions (Appendix I.2). GeoPFN coverage was 0.901, closest to nominal among the Table 4 models. Per-field REML kriging had similar coverage (0.902) but 37% wider intervals (3.77 versus 2.76) and higher CRPS and NLL; at similar coverage, the narrower intervals of GeoPFN therefore represent more concentrated predictive distributions.

Table 4. Scores and inference times on the 120 matched fields (10 per class) under the 36 conditions of Table 3. RMSE, CRPS and interval width are in $\log_{10} K$*. GPU times (ms per field) are means over 12 class representatives and six sensor counts at* $\sigma = 0.2$*; TabPFN times include both fitting and prediction under its default GPU mixed precision. GeoPFN and GeoPFN-V times include CPU inputs and outputs; TabPFN and kriging times exclude transfers. Bold marks the best score (for coverage, the value closest to 0.90) and the shortest time. The timing protocol is described in Appendix I.2.*

Model	RMSE ↓	CRPS ↓	NLL ↓	Cov. 90	Width 90 ↓	Inference time ↓ (ms/field)
GeoPFN (this study)	**1.427**	**0.574**	0.758	**0.901**	**2.76**	17
GeoPFN-V	**1.427**	**0.574**	**0.746**	0.895	**2.76**	**14**
TabPFN-3.5	1.516	0.648	0.940	0.917	3.70	730
TabPFN-3.5 (with σ)	1.495	0.628	0.924	0.917	3.61	750
Kriging, global prior	1.452	0.681	1.166	0.910	4.29	20
Kriging, class prior (oracle)	1.440	0.666	1.119	0.903	4.10	20
Kriging, per-field REML	1.435	0.649	1.097	0.902	3.77	725

Calibration across interval levels. GeoPFN's 50% interval covered 48.4%, and its PIT histogram was nearly uniform. Kriging's 50% intervals covered 61–64%, indicating over-dispersion near the

distribution centre (Appendix Figure D.2). The 120-field comparison showed the same pattern for GeoPFN; TabPFN-3.5's 50% interval covered 59.8% (Figure 15).

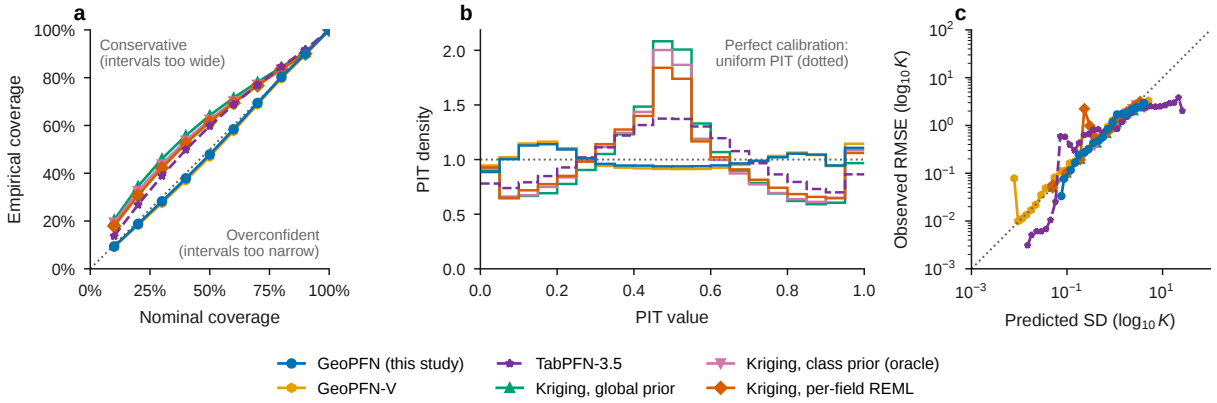


Figure 15. Probabilistic calibration of the probabilistic models on the 120 matched fields of Table 4. (a) Empirical coverage of central prediction intervals against their nominal level; (b) PIT density; (c) observed RMSE against predicted standard deviation. Dotted lines indicate ideal probabilistic calibration. GeoPFN-V predicts a single total variance instead of separate structural and measurement components. The same diagnostics for the 1,200-field benchmark are shown in Appendix Figure D.2.

Figure 16 shows six of these models on the layers field of Figure 2 (256 observations, $\sigma = 0.3$). GeoPFN preserves the two main contacts, which the standard local TabPFN-3.5 mean smooths out (RMSE 0.576 versus 0.686).

6. Discussion

GeoPFN reconstructs clean hydraulic-conductivity fields from observations on irregular sensor layouts and a supplied noise level. On 1,200 paired synthetic fields, it achieved 0.900 pooled 90% coverage; relative to per-field REML kriging, CRPS was 13% lower (0.591 versus 0.677) and mean interval width was 28% narrower (2.81 versus 3.92). RMSE was similar (1.499 versus 1.509). GPU inference for a 64 × 64 field took 13–33 ms, depending on sensor count. Because each update requires only one forward pass of the trained network, with neither retraining nor per-field covariance fitting, GeoPFN is a fast computational component for probabilistic conductivity mapping under the tested synthetic prior. The sequential sensor-placement example in Section 5.4 illustrates repeated prediction updates, but it does not establish a better investigation strategy.

Meaning of the variance split. The labels *structural* and *measurement* describe the input dependencies imposed by the architecture. The structural component responds to observations

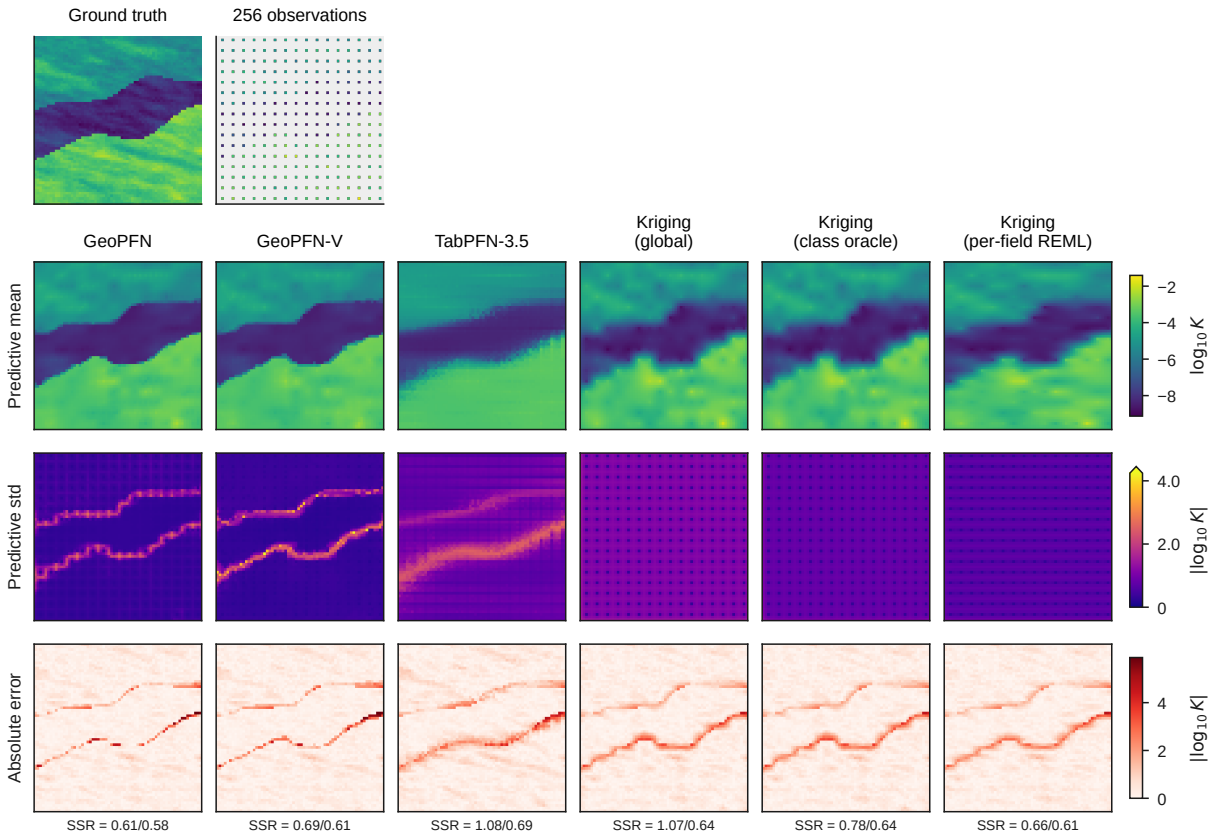


Figure 16. Predictions of six probabilistic models for one held-out layers field observed at the same 256 locations ($\sigma = 0.3$). The top row shows the clean target and the observations; the following rows show the predictive mean, the predictive standard deviation and the absolute error of each model. The labels below the panels give the root-mean predictive standard deviation and the RMSE over all 4,096 cells, whose ratio is the SSR. For GeoPFN, the standard deviation is $\sqrt{S_q + M_q}$; GeoPFN-V predicts a single variance. Standard deviations above $\sqrt{18} \approx 4.24$ are saturated in the colour scale. The TabPFN panel uses the same local TabPFN-3.5 checkpoint and inference settings as Table 4.

and sensor geometry and often highlights contacts; the measurement component responds to sensor layout and the supplied noise level. These are operationally distinct maps, not uniquely identified physical uncertainty sources. The predictive likelihood depends on their sum, so it cannot identify the split. Moreover, the measurement component remains nonzero at zero supplied noise and increases with sensor sparsity, indicating that it can also absorb geometry-dependent interpolation error. We therefore interpret the maps as model diagnostics for field structure and measurement conditions, not as a physical decomposition.

Predictive value and calibration. The matched GeoPFN-V ablation achieved slightly better pooled RMSE, CRPS and NLL than GeoPFN, while GeoPFN had coverage closer to nominal and marginally narrower intervals. The variance split therefore provides two diagnostic maps

with little change in pooled predictive performance, without improving accuracy. Its practical appeal lies in interpretation: in the illustrative example of Figure 1 and Appendix Figure B.1, the structural map highlights contacts more clearly than the single total-variance map of GeoPFN-V, which combines structure- and measurement-related variance. This comparison is qualitative and was not quantified across the test set. GeoPFN-V covered more unsensed boundary cells than GeoPFN (0.774 versus 0.744), whereas GeoPFN had higher coverage under several clustered and survey-line layouts. Both models nevertheless undercovered substantially at boundaries and under spatially correlated errors. Because the comparison rests on a single training seed, it supports descriptive differences rather than a general advantage across sensor layouts and error processes. Pooled calibration was close to nominal, but subgroup performance was not: 90% intervals covered 74.4% of unsensed boundary cells in the paired benchmark, compared with 91.8% of unsensed interior cells. Boundary undercoverage is a central limitation because contacts motivate the use of spatially resolved uncertainty maps.

Scope and limitations. Training and primary evaluation used one 12-class synthetic conductivity generator, with one training seed for each neural model. The TabPFN-3.5 comparison used only 120 fields and unequal access to prior and noise information; it is exploratory and does not establish a general model ranking. The sequential-placement example on six selected fields shows that GeoPFN also accommodates irregular sensor layouts that expand one sensor at a time; it does not assess the value of information or a geotechnical limit state. Its pointwise predictive distributions do not specify the spatial dependence needed to propagate conductivity uncertainty through a seepage or reliability analysis. Inference timings exclude data preparation and transfer. No measured-site data, property-transformation model or engineering response calculation was evaluated. Consequently, neither transfer to field sites nor an engineering decision benefit of the maps has been demonstrated.

Engineering interpretation. Spatially uncertain conductivity is relevant to seepage through embankments and foundations (Cho, 2012; Liu et al., 2017). A calibrated conductivity model could eventually provide input to such analyses, but the present pointwise predictions cannot be interpreted as seepage-flow or failure-probability forecasts. Before using them in reliability engineering, the spatial dependence of the field, hydraulic boundary conditions, geometry and

limit state must be specified and validated. In particular, the boundary undercoverage reported here concerns the very contacts that can govern preferential flow.

Future work. Evaluation on independent geological priors and measured conductivity data, with multiple training seeds, is needed to assess generalisation and uncertainty calibration. Direct tests or a validated transformation from indirect observations would be required to establish an observation model for a real site. Further matched ablations could test the contribution of noise conditioning and the stability of the variance split. Extensions to unknown or sensor-specific noise and joint field predictions would relax the current modelling assumptions. Prospective comparisons with conventional investigation layouts and decision-specific seepage analyses are needed to determine whether the maps improve engineering outcomes.

7. Conclusions

Sparse, noisy measurements can miss geological contacts and obscure the value of further investigation. GeoPFN combines observations on irregular sensor layouts with a known noise level to predict a clean hydraulic-conductivity field in one GPU forward pass, together with two constrained variance maps with different input responses. These properties support rapid probabilistic conductivity mapping in the tested synthetic setting.

On held-out fields from the synthetic prior, GeoPFN was probabilistically well calibrated in aggregate: the empirical coverage of its central predictive intervals closely matched the nominal level from 50% to 95% (0.479, 0.8975 and 0.939 for nominal 50%, 90% and 95% intervals), and its probability integral transform histograms were nearly uniform. Relative to per-field REML kriging, it reduced CRPS by 13% and 90% interval width by 28%, with similar coverage; a matched single-variance ablation had slightly better pooled scores. The variance split therefore provides diagnostic maps with little difference in predictive performance rather than a gain in accuracy. Coverage was substantially lower at unsensed boundaries. The structural map often highlighted incompletely sampled contacts, channels and lenses, while the measurement map reflected sensor layout and supplied noise level.

Evaluation on independent priors and measured sites, with multiple training seeds, is needed to

establish transfer and calibration. The current synthetic evidence does not establish a reliable conductivity map for any particular field site or a benefit in seepage or reliability assessment. Further work should test unknown or sensor-specific noise, joint field predictions and the value of uncertainty-guided measurement placement against established survey designs.

Data and code availability

The following are openly available on Zenodo: the training, validation and test fields (Geoprior 2-D dataset, v1.0.0; https://doi.org/10.5281/zenodo.23975277), the code of the generator that produced them (Geoprior v1.0.0; https://doi.org/10.5281/zenodo.23984677) and the GeoPFN and GeoPFN-V code with trained weights (v1.0.0; https://doi.org/10.5281/zenodo.23984593). Baseline implementations, evaluation scripts and figure data are available from the corresponding author on reasonable request.

Declaration of competing interests

The authors declare no competing interests.

Author contributions: CRediT

Sopheakpolin Mom: Conceptualization, Methodology, Software (geological prior and GeoPFN development), Writing – original draft, Writing – review and editing. Yu Otake: Conceptualization, Funding acquisition, Supervision, Writing – review and editing. Stephen Wu: Conceptualization, Supervision, Writing – review and editing.

References

Amini, A., Schwarting, W., Soleimany, A., Rus, D., 2020. Deep evidential regression. Adv. Neural Inf. Process. Syst. 33, 14927–14937. https://proceedings.neurips.cc/paper/2020/hash/aab085461de182608ee9f607f3f7d18f-Abstract.html.

Bouayach, N., Kassou, F., Rguig, M., 2025. 3D combined stratigraphy and geo-properties modeling using probabilistic machine learning. Eng. Geol. 357, 108387. https://doi.org/10.101

6/j.enggeo.2025.108387.

Chen, W., Ding, J., Wang, T., Connolly, D.P., Wan, X., 2023. Soil property recovery from incomplete in-situ geotechnical test data using a hybrid deep generative framework. Eng. Geol. 326, 107332. https://doi.org/10.1016/j.enggeo.2023.107332.

Ching, J., Phoon, K.K., 2017. Characterizing uncertain site-specific trend function by sparse Bayesian learning. J. Eng. Mech. 143 (7), 04017028. https://doi.org/10.1061/(ASCE)EM.1943-7889.0001240.

Ching, J., Kamyab Farahbakhsh, H., Wang, J.-S., Li, X., Wang, H., 2026. Fully coupled conditional simulation of geological and geotechnical variabilities for sparse geotechnical data in three dimensions. Eng. Geol. 364, 108609. https://doi.org/10.1016/j.enggeo.2026.108609.

Cho, S.E., 2012. Probabilistic analysis of seepage that considers the spatial variability of permeability for an embankment on soil foundation. Eng. Geol. 133–134, 30–39. https://doi.org/10.1016/j.enggeo.2012.02.013.

Cressie, N.A.C., 1993. Statistics for Spatial Data, rev. ed. Wiley, New York. https://doi.org/10.1002/9781119115151.

Fortin, V., Abaza, M., Anctil, F., Turcotte, R., 2014. Why should ensemble spread match the RMSE of the ensemble mean? J. Hydrometeorol. 15 (4), 1708–1713. https://doi.org/10.1175/JHM-D-14-0008.1.

Garnelo, M., Rosenbaum, D., Maddison, C., Ramalho, T., Saxton, D., Shanahan, M., Teh, Y.W., Rezende, D., Eslami, S.M.A., 2018. Conditional neural processes, in: Proceedings of the 35th International Conference on Machine Learning. Proc. Mach. Learn. Res. 80, 1704–1713. https://proceedings.mlr.press/v80/garnelo18a.html.

Gneiting, T., Raftery, A.E., 2007. Strictly proper scoring rules, prediction, and estimation. J. Am. Stat. Assoc. 102 (477), 359–378. https://doi.org/10.1198/016214506000001437.

Gong, W., Zhao, C., Juang, C.H., Zhang, Y., Tang, H., Lu, Y., 2021. Coupled characterization of stratigraphic and geo-properties uncertainties – A conditional random field approach. Eng. Geol. 294, 106348. https://doi.org/10.1016/j.enggeo.2021.106348.

Hollmann, N., Müller, S., Purucker, L., Krishnakumar, A., Körfer, M., Hoo, S.B., Schirrmeister, R.T., Hutter, F., 2025. Accurate predictions on small data with a tabular foundation model. Nature 637, 319–326. https://doi.org/10.1038/s41586-024-08328-6.

Jäger, B., Erickson, N., Grinsztajn, L., Birkel, F., Flöge, K., Key, O., Kaya, K., Kübler, J., Frankel, A., Schröder, T., Garg, A., Metzen, J.H., Salinas, D., Bing, S., Collins, K., Çelik, T., Balazadeh, V., Sidhoum, L., Pereda, T., Roof, B., Tschalzev, A., Guo, S., Singer, P., Purucker, L., Robertson, J., Salmon, M., Jund, P., Chen, J., Kriuchkova, D., Cahu, A., Kalfon, E., Hayler, A., Grab, G., Monteiro, V., Wehrhahn, L., Safaric, D., Cornu, C., Arazi, A., Grace, R., Alessi, S., Manium, M., Schölkopf, B., LeCun, Y., Hulsebos, M., Gambhir, S., Hollmann, N., Hutter, F., 2026. TabPFN-3.5: Technical report. arXiv preprint arXiv:2609.17895. https://doi.org/10.48550/arXiv.2609.17895.

Laloy, E., Hérault, R., Jacques, D., Linde, N., 2018. Training-image based geostatistical inversion using a spatial generative adversarial neural network. Water Resour. Res. 54 (1), 381–406. https://doi.org/10.1002/2017WR022148.

Lee, J., Lee, Y., Kim, J., Kosiorek, A., Choi, S., Teh, Y.W., 2019. Set Transformer: A framework for attention-based permutation-invariant neural networks, in: Proceedings of the 36th International Conference on Machine Learning. Proc. Mach. Learn. Res. 97, 3744–3753. https://proceedings.mlr.press/v97/lee19d.html.

Li, X., Zhang, Y., Li, Z., Yang, Z., Qi, X., 2025. A coupled probabilistic site characterization method for estimating soil stratification and spatial variability using multiple-source site investigation data. Eng. Geol. 351, 108024. https://doi.org/10.1016/j.enggeo.2025.108024.

Liu, K., Vardon, P.J., Hicks, M.A., Arnold, P., 2017. Combined effect of hysteresis and heterogeneity on the stability of an embankment under transient seepage. Eng. Geol. 219, 140–150. https://doi.org/10.1016/j.enggeo.2016.11.011.

Meinert, N., Gawlikowski, J., Lavin, A., 2023. The unreasonable effectiveness of deep evidential regression. Proc. AAAI Conf. Artif. Intell. 37 (8), 9134–9142. https://doi.org/10.1609/aaai.v37i8.26096.

Müller, S., Hollmann, N., Pineda Arango, S., Grabocka, J., Hutter, F., 2022. Transformers can do Bayesian inference, in: Proceedings of the 10th International Conference on Learning Representations (ICLR 2022). https://openreview.net/forum?id=KSugKcbNf9.

Otake, Y., Honjo, Y., 2022. Challenges in geotechnical design revealed by reliability assessment: Review and future perspectives. Soils Found. 62 (3), 101129. https://doi.org/10.1016/j.sandf.2022.101129.

Otake, Y., Kodama, S., Watanabe, S., 2019. Improvement in the information-oriented construction of temporary soil-retaining walls using sparse modeling. Undergr. Space 4 (3), 210–224. https://doi.org/10.1016/j.undsp.2018.12.004.

Park, S.W., Linsen, L., Kreylos, O., Owens, J.D., Hamann, B., 2006. Discrete Sibson interpolation. IEEE Trans. Vis. Comput. Graph. 12 (2), 243–253. https://doi.org/10.1109/TVCG.2006.27.

Patterson, H.D., Thompson, R., 1971. Recovery of inter-block information when block sizes are unequal. Biometrika 58 (3), 545–554. https://doi.org/10.1093/biomet/58.3.545.

Phoon, K.K., Kulhawy, F.H., 1999. Characterization of geotechnical variability. Can. Geotech. J. 36 (4), 612–624. https://doi.org/10.1139/t99-038.

Phoon, K.K., Cao, Z.J., Ji, J., Leung, Y.F., Najjar, S., Shuku, T., Tang, C., Yin, Z.Y., Yoshida, I., Ching, J., 2022a. Geotechnical uncertainty, modeling, and decision making. Soils Found. 62 (5), 101189. https://doi.org/10.1016/j.sandf.2022.101189.

Phoon, K.K., Ching, J., Shuku, T., 2022b. Challenges in data-driven site characterization. Georisk 16 (1), 114–126. https://doi.org/10.1080/17499518.2021.1896005.

Qian, Z., Shi, C., 2026. An implicit feature learning approach for automatic digital twinning of three-dimensional subsurface stratigraphy from limited boreholes. Eng. Geol. 363, 108568. https://doi.org/10.1016/j.enggeo.2026.108568.

Roberts, D.R., Bahn, V., Ciuti, S., Boyce, M.S., Elith, J., Guillera-Arroita, G., Hauenstein, S., Lahoz-Monfort, J.J., Schröder, B., Thuiller, W., Warton, D.I., Wintle, B.A., Hartig, F., Dormann, C.F., 2017. Cross-validation strategies for data with temporal, spatial, hierarchical, or phylogenetic structure. Ecography 40 (8), 913–929. https://doi.org/10.1111/ecog.02881.

Saito, T., Otake, Y., Wu, S., 2026. Applying a tabular foundation model to geotechnical site characterization. Geodata AI 6, 100040. https://doi.org/10.1016/j.geoai.2025.100040.

Shepard, D., 1968. A two-dimensional interpolation function for irregularly-spaced data, in: Proceedings of the 1968 23rd ACM National Conference. ACM, New York, pp. 517–524. https://doi.org/10.1145/800186.810616.

Strebelle, S., 2002. Conditional simulation of complex geological structures using multiple-point statistics. Math. Geol. 34 (1), 1–21. https://doi.org/10.1023/A:1014009426274.

Tancik, M., Srinivasan, P., Mildenhall, B., Fridovich-Keil, S., Raghavan, N., Singhal, U., Ramamoorthi, R., Barron, J., Ng, R., 2020. Fourier features let networks learn high frequency functions in low dimensional domains. Adv. Neural Inf. Process. Syst. 33, 7537–7547. https://papers.neurips.cc/paper_files/paper/2020/hash/55053683268957697aa39fba6f231c68-Abstract.html.

Wang, Y., Cao, Z., Li, D., 2016. Bayesian perspective on geotechnical variability and site characterization. Eng. Geol. 203, 117–125. https://doi.org/10.1016/j.enggeo.2015.08.017.

Yoshida, I., Tasaki, Y., Otake, Y., Wu, S., 2018. Optimal sampling placement in a Gaussian random field based on value of information. ASCE-ASME J. Risk Uncertain. Eng. Syst. Part A: Civ. Eng. 4 (3), 04018018. https://doi.org/10.1061/AJRUA6.0000970.

Yoshida, I., Tomizawa, Y., Otake, Y., 2021. Estimation of trend and random components of conditional random field using Gaussian process regression. Comput. Geotech. 136, 104179. https://doi.org/10.1016/j.compgeo.2021.104179.

Zhao, C., Gong, W., Juang, C.H., Tang, H., Hu, X., Wang, L., 2023. Optimization of site exploration program based on coupled characterization of stratigraphic and geo-properties uncertainties. Eng. Geol. 317, 107081. https://doi.org/10.1016/j.enggeo.2023.107081.

Zhou, X., Shi, P., Wu, G., 2026. Multi-scale reconstruction of 3D subsurface model using deep learning techniques based on cone penetration testing data. Eng. Geol. 369, 108793. https://doi.org/10.1016/j.enggeo.2026.108793.

Appendices

These appendices provide the methods and condition-level evidence that support the main text. Appendices A–C specify the generator, model and evaluation protocols; Appendices D–H report comparative and stress-test results; Appendix I documents timing and reproducibility; Appendix J summarises the principal calibration failures.

Evaluation sets and conventions. Three evaluation sets are used. The *full test set* comprises all 5,000 held-out fields under 66 conditions (6 sensor counts × 11 noise levels), with two noise draws per condition; it underlies the full-test results of the main text and the overview in Appendix E. The *paired benchmark* comprises 1,200 held-out fields, namely the first 100 task IDs of each of the 12 classes, under 36 conditions (6 sensor counts × 6 noise levels) with one noise draw per condition. All models receive the same fields, layouts and noise draws, and this benchmark is used in Appendices D–H unless stated otherwise. The *matched TabPFN set* consists of the first ten fields of each class in the paired benchmark (120 fields) and is used for Table 4 and Figure 15. GeoPFN is the proposed model and GeoPFN-V is its matched single-variance ablation (Section B.4); the three kriging variants and three point interpolators are specified in Section C.2.

Throughout, $Y = \log_{10}[K/(1\,\mathrm{m\,s^{-1}})]$. Because a cell is not an independent replicate, confidence intervals are obtained by resampling whole fields within geological classes. In the score tables, bold marks the lowest error or the coverage closest to the nominal level unless the caption states otherwise.

Appendix contents

Appendix	Contents
A	Geological prior: natural analogues, class geometry and material distributions
B	Architecture: attention, output transforms, predictive distribution, response guarantees and the GeoPFN-V ablation

Appendix	Contents
C	Protocols: training and selection, comparative and stress-test designs, metrics and resampling
D	Pooled and per-sensor-count comparison, calibration across probability levels and exceedance forecasts
E	Boundary, sensor-status, class and material diagnostics; selection of the qualitative examples
F	Repeated random layouts and structured sensor layouts
G	Non-Gaussian, correlated and biased sensor errors; sensitivity to the supplied noise level
H	Estimating an unknown noise level from the sensors
I	Latency, the same-session timing of Table 4, and computational cost
J	Conditions in which calibration fails

Appendix A. Geological prior

The prior generator produces synthetic fields in 12 classes representing broad plan-view patterns of layers, channels, lenses, weathered rock, faults, fractures and karst-like features (Table A.1). These analogues illustrate geometry only; the generator neither simulates site formation nor infers class frequencies and hydraulic properties from natural sites.

Table A.1. Natural settings that the 12 synthetic classes are intended to resemble. The analogues describe geometric patterns only; they are not classifications of real sites.

Generator class	Natural analogue
`layers`	Contrasting coarse and fine sediment beds
`graded_bedding`	Fining or coarsening sediment cycles
`cross_bedded`	Inclined sand laminae
`unconformity`	Erosional truncation beneath younger sediment
`channel`	Buried sand or gravel channel in valley fill
`channel_network`	Connected channel fills in alluvium
`lens_field`	Discontinuous sand or gravel lenses in fine deposits
`weathered_bedrock`	Weathering mantle above fractured bedrock
`fault`	Fault core and surrounding damage zone
`fracture_network`	Water-bearing bedrock fractures
`intrusion`	Dyke or sill with altered contacts
`karst_proxy`	Dissolution conduits and cavities

Table A.2 lists the main sampled geometry parameters, and Table A.3 lists the default material properties. Beds and weathering are plan-view patterns rather than vertical profiles, and `karst_proxy` is a conductivity pattern rather than a discrete-conduit flow model. The complete sampling procedure is defined in the generator code described under Data and code availability.

Table A.2. Main geometry parameters of each generator class. Counts refer to one field, and lengths are given as fractions of the domain extent. Each value is either a sampling range or a fixed setting, as indicated.

Class	Main pattern	Principal sampled values
`layers`	Alternating beds	3–6 bands; dip −0.28 to 0.28 rad; contact waviness 0.030–0.060.
`graded_bedding`	Fining or coarsening bands	2–4 cycles of 3–4 sub-bands.
`cross_bedded`	Beds with inclined laminae	3–6 bands; lamina spacing 0.06–0.11.

Class	Main pattern	Principal sampled values
`unconformity`	Older beds cut by erosion, then capped	3–6 older bands; erosional amplitude 0.10; cap width 0.12.
`channel`	One sinuous high-conductivity body	Width 0.05–0.12; meander amplitude 0.03–0.10.
`channel_network`	A trunk with branches	2–3 branches; trunk width as in `channel`.
`lens_field`	High- or low-conductivity ellipses	3–7 lenses; size scale 0.06–0.14.
`weathered_bedrock`	Three weathering labels	Gaussian-field range 0.22; labels split at the 35th and 75th percentiles.
`fault`	Displaced beds with a sealing or conducting zone	Throw 0.06–0.18; zone half-width 0.02–0.05.
`fracture_network`	Conducting finite fractures	5–11 fractures; radius 0.15–0.45; half-width 0.01–0.03.
`intrusion`	A dyke or sill with a contact aureole	Sheet half-width 0.03–0.07; aureole extends to 2.2 times this width.
`karst_proxy`	One conduit with high-conductivity cavities	3–6 cavities; conduit width 0.05–0.10; cavity radii 0.03–0.09.

Table A.3. Material roles used by the generator, with the default mean $\mu_m^{(0)}$ and the within-material standard deviation σ_m of Y in $\log_{10} K$ units. The roles are labels inside the generator and are not soil or rock classifications.

ID	Generator role	$\mu_m^{(0)}$	σ_m
0	Background	−5.2	0.45
1	Fines or seal	−8.0	0.35
2	Sand	−3.6	0.40
3	Gravel or conduit	−2.1	0.35
4	Intact rock	−8.5	0.25
5	Weathered zone	−5.8	0.50
6	Low-conductivity anomaly	−8.5	0.25
7	High-conductivity anomaly	−1.7	0.30

For each field, a shared contrast factor (0.7–1.35) and independent normal mean shifts (standard deviation 0.3) perturb the Table A.3 means. Each connected body has macro- and microscale Gaussian residuals with correlation ranges of approximately 0.02–0.85 and 0.015–0.05 of the domain extent, respectively. The generator samples nine covariance families, including exponential, Matérn and Gaussian. Final values are clipped to $Y \in [-12, 0]$, equivalent to $K \in [10^{-12}, 1]$ m/s. These parameter choices generate variability within the synthetic prior and were not calibrated against the analogues in Table A.1.

Appendix B. Architecture and parameterisation

The main text defines the observation task, the variance split, the predictive distribution and the training objective. This appendix specifies the network and its output transforms. Coordinates lie in $[0, 1]^2$; standard evaluations query the 4,096 cell centres of a 64 × 64 field. The model has a width of 256 and eight attention heads of dimension 32.

Table B.1. Layers and trainable parameters of GeoPFN. The observation head produces m_q, a_q and ν_q, and the geometry head produces $M_{0,q}$ and τ_q. Dropout in the encoder is zero.

Module	Specification	Trainable parameters
Fourier features	Fixed 2×64 frequencies; 128 sine/cosine outputs	0
Sensor embedding	$130 \to 256 \to 256$, GELU	99,328
Sensor encoder	Four pre-LayerNorm self-attention layers without positional order, as in set attention (Lee et al., 2019); eight heads; feed-forward width 1,024; final LayerNorm	3,159,552
Query embedding	$128 \to 256 \to 256$, GELU	98,816
Query decoder	Three spatial cross-attention blocks; eight heads; feed-forward width 1,024	2,369,304
Observation head	LayerNorm then $256 \to 3$	1,283
Geometry head	$130 \to 256 \to 2$, GELU	34,050
Total		5,762,333

B.1 Attention and output transforms

Sensors and queries use the same fixed Fourier coordinate features, which facilitate the representation of sharp and oblique boundaries (Tancik et al., 2020):

$$\phi(\mathbf{x}) = [\sin(2\pi W^\top \mathbf{x}), \cos(2\pi W^\top \mathbf{x})], \qquad W_{ij} \sim \mathcal{N}(0, 8^2), \tag{B.1}$$

The 64 frequency vectors are drawn once (seed 0), yielding 128 features. A sensor embedding concatenates $\phi(\mathbf{x}_i)$, the standardised reading $(Z_i - \bar{y})/s_y$ and the standardised noise level σ/s_y. A multilayer perceptron projects this vector to width 256, and four Transformer layers encode the sensor set. Queries use a separate embedding of their Fourier features. In cross-attention block r, head h weights sensor i for query $\mathbf{q}$ by

$$\alpha_{qi}^{(r,h)} = \mathrm{softmax}_i\left[\frac{\mathbf{u}_{q,h}^{\top}\mathbf{v}_{i,h}}{\sqrt{32}} - \exp(\kappa_{r,h})\|\mathbf{q}-\mathbf{x}_i\|^2\right]. \tag{B.2}$$

The first term compares learned query and sensor features, whereas the second favours nearby sensors. Each head computes a weighted sum of sensor value projections, followed by an output projection, residual update and pre-normalised $256 \to 1024 \to 256$ GELU feed-forward update. Head log precision is initialised as $\kappa_h = -\log(2L_h^2)$, with L_h logarithmically spaced from $1/64$ to 0.5. Jointly permuting sensor coordinates and readings leaves predictions unchanged up to numerical rounding. Because there is no query-to-query attention, predictions are independent of the other locations queried. Sensor embeddings and the Fourier features of a fixed query set can be cached, although both are recomputed in the timings of Appendix I.

A linear observation head maps the decoded query representation to raw mean, structural-amplitude and tail outputs. The mean is $m_q = \bar{y} + s_y o_{\mathrm{mean},q}$, where $\bar{y}$ and s_y are the training-split mean and standard deviation of Y, and the structural amplitude is $a_q = \mathrm{sigmoid}(o_{\mathrm{str},q})$. The distance gate of the structural variance carries no information about the field, whereas the amplitude depends on the readings; consequently, the structural variance between sensors can follow the observed structure. The mean remains a learned estimate of the clean value, even at a noisy sensor.

The geometry head receives $[\phi(\mathbf{q}), d_q, \log(1+N)/\log(1+4096)]$ but neither the readings nor σ. Consequently, for fixed weights and a fixed layout, $M_{0,q}$ and τ_q cannot depend on the readings or on the supplied noise level. Raw outputs $o_{M,q}$ and $o_{\tau,q}$ are transformed as

$$\begin{aligned} M_{0,q} &= M_{\min} + (M_{\max} - \Delta_M - M_{\min})\,\mathrm{sigmoid}(o_{M,q}), \\ \tau_q &= \tau_{\min} + (\tau_{\max} - \tau_{\min})\,\mathrm{sigmoid}(o_{\tau,q}). \end{aligned} \tag{B.3}$$

The constants are $M_{\min} = S_{\min} = 10^{-4}$ (standard deviation 0.01), $M_{\max} = S_{\max} = 18$, $\Delta_M = 0.01$, $\tau_{\min} = 0.05$, $\tau_{\max} = 10$ and $\ell = 4/64$. The margin Δ_M ensures that $M_{\max} - M_{0,q} \geq 0.01$, thereby preventing a flat noise response. The gate length ℓ corresponds to four grid cells. These values are design choices rather than fitted physical constants. The measurement variance equals

$M_{0,q}$ at $\sigma = 0$ and lies halfway between $M_{0,q}$ and $M_{\max}$ at $\sigma = \tau_q$. The bound $V_q \le 36$ is the maximum variance of a variable confined to the prior's 12-unit $\log_{10} K$ range; the Student-t predictive distribution itself is unbounded.

The derivative of the measurement variance in Eq. (3),

$$\frac{\partial M_q}{\partial \sigma} = (M_{\max} - M_{0,q}) \frac{2\sigma\tau_q^2}{(\sigma^2 + \tau_q^2)^2} > 0 \qquad (\sigma > 0), \tag{B.4}$$

is positive because $M_{\max} > M_{0,q}$ and $\tau_q > 0$. For $\sigma \ll \tau_q$, $M_q \approx M_{0,q} + (M_{\max} - M_{0,q})\sigma^2/\tau_q^2$; that is, the response initially scales with the noise variance. For identical sensor geometry and supplied noise, two fields therefore yield identical measurement maps, although their predictive means and structural maps may differ.

B.2 Predictive distribution and negative log likelihood

Integrating μ_q and ω_q^2 out of the NIG hierarchy in Eq. (5) gives

$$Y(\mathbf{q}) \mid D \sim t_{2\alpha_q}\left(m_q, \frac{\beta_q(1+\lambda_q)}{\lambda_q \alpha_q}\right), \qquad M_q = \frac{\beta_q}{\alpha_q - 1}, \qquad S_q = \frac{\beta_q}{\lambda_q(\alpha_q - 1)}. \tag{B.5}$$

The network predicts m_q, M_q, S_q and $\nu_q = 2.1 + \mathrm{softplus}(o_{\mathrm{tail},q})$. The equivalent NIG parameters

$$\alpha_q = \frac{\nu_q}{2}, \qquad \lambda_q = \frac{M_q}{S_q}, \qquad \beta_q = (\alpha_q - 1)M_q \tag{B.6}$$

return $\mathbb{E}[\omega_q^2 \mid D] = M_q$ and $\mathrm{Var}[\mu_q \mid D] = S_q$, and the marginal becomes $t_{\nu_q}(m_q, s_q^2)$ with $s_q^2 = V_q(\nu_q - 2)/\nu_q$. The variance floors and ceilings bound λ_q; $M_q > 0$ and $\alpha_q > 1$ ensure $\beta_q > 0$.

For each query, the expected NLL under the generative prior decomposes as

$$\mathbb{E}_{D,Y}[-\log p_\theta(Y(\mathbf{q}) \mid D, \mathbf{q})] = \mathbb{E}_D[\mathrm{KL}(p(\cdot \mid D, \mathbf{q}) \,\|\, p_\theta(\cdot \mid D, \mathbf{q}))] + \mathbb{E}_D[\mathscr{H}(p(\cdot \mid D, \mathbf{q}))], \tag{B.7}$$

where $p(\cdot \mid D, \mathbf{q})$ is the posterior predictive distribution implied by the prior and its entropy $\mathscr{H}$ does not depend on θ. For one query with clean value y and residual $e_q = y - m_q$, the Student-t NLL is

$$-\log p_\theta(y) = \log \frac{\Gamma(\nu_q/2)}{\Gamma\big((\nu_q+1)/2\big)} + \frac{1}{2}\log(\nu_q \pi s_q^2) + \frac{\nu_q+1}{2}\log\left(1 + \frac{e_q^2}{\nu_q s_q^2}\right), \tag{B.8}$$

which depends on M_q and S_q only through V_q.

B.3 Scope of the response guarantees

Training uses the Student-t likelihood directly; the NIG parameters constitute an equivalent description and are not computed during training. Table B.2 summarises the response properties that follow from the formulas.

Table B.2. Response properties of the variance components that follow from the architecture, and the scope of each guarantee. Properties that the formulas do not guarantee, including probabilistic calibration and the physical meaning of each component, must be assessed empirically.

Property	Scope
Structural variance equals its floor at a sensor	Guaranteed by $d_q = 0$
Measurement variance rises with $\sigma > 0$	Guaranteed for fixed weights and layout
Total variance rises with σ at a sensor	Structural variance is fixed there
Total variance rises with σ away from sensors	Not guaranteed; structural variance can change
Predictive interval width rises with σ	Not guaranteed; tail weight can change
Calibration or physical identification of the components	Not implied by the formulas

At an exactly sensed, noise-free location, the ideal clean-field conditional law is degenerate; the

positive variance floors maintain a continuous approximation. The model provides marginal distributions rather than a joint spatial law. Transformed quantiles yield conductivity quantiles, and 10^{m_q} is the conductivity median. An untruncated finite-degree Student-t in log conductivity has no finite positive exponential moment, so estimating mean conductivity or sampling whole fields requires additional modelling assumptions.

B.4 Matched ablation: GeoPFN-V

GeoPFN-V examines the effect of the constrained variance head (Figure B.1). It retains GeoPFN's encoder–decoder backbone, Fourier features, noise input, mean and degrees-of-freedom outputs, Student-t NLL, paired noise views, data, training schedule and checkpoint-selection rule. It removes the geometry head, distance gate, noise-response formula and component bounds; the observation head instead outputs $V_q = \text{softplus}(r_q) + 10^{-6}$, with the constant ensuring numerical positivity. Under the same seed, the shared parameters are initialised with identical values. GeoPFN-V has 5,728,283 trainable parameters versus GeoPFN's 5,762,333; their selected checkpoints are at steps 1,620,000 and 1,505,000, respectively. Because both models receive σ, this ablation does not test noise conditioning.

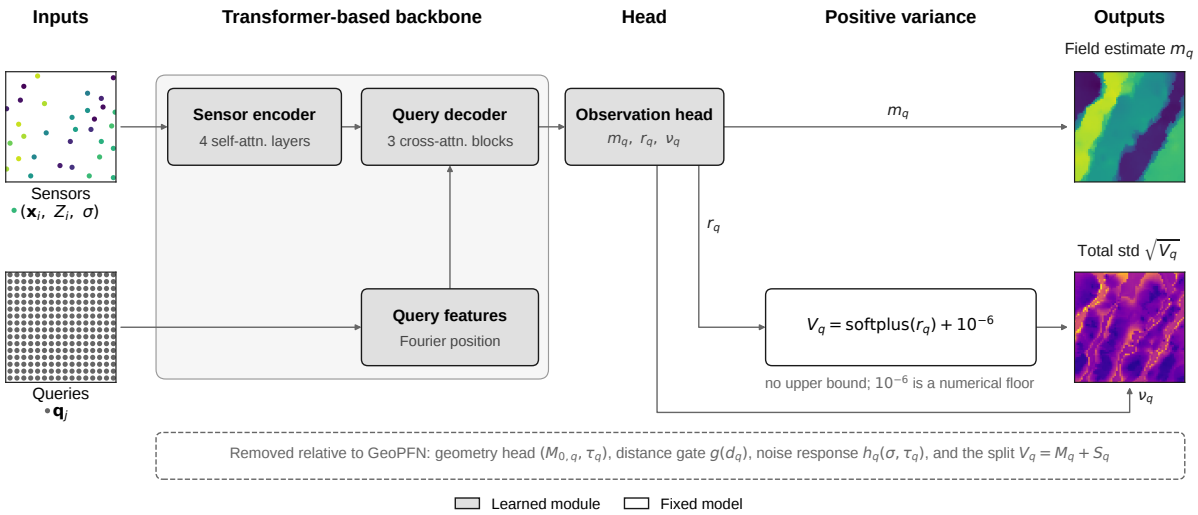


Figure B.1. Architecture of the GeoPFN-V ablation, drawn in the same way as Figure 1 and shown with the same illustrative inputs. The dashed box lists the components removed from GeoPFN. GeoPFN-V outputs a single predictive standard deviation, whose map has its own colour scale. Grey boxes denote learned modules, and white boxes denote fixed operations. Attn., attention.

Appendix C. Training and evaluation protocols

C.1 Training, selection and full-test protocol

Training schedule and selection. Training minimises mean Student-t NLL against clean target cells. Each optimiser step uses two fields (batch size 2) and two noise views per field. The views share the clean field, sensor layout and standardised Gaussian draw but use different noise levels: one scheduled value in $\{0, 0.05, 0.1, 0.2, 0.5, 1\}$ and one drawn uniformly from $[0, 1]$. The two NLLs are averaged before a single update. No pairwise consistency loss is used, and the effect of the pairing was not isolated.

The seed-0 schedule visits each of 90,000 training fields once at each of six sensor counts $N \in \{4, 16, 64, 256, 1024, 4096\}$ and six scheduled noise levels: $90{,}000 \times 36/2 = 1{,}620{,}000$ optimiser steps. Layouts and noise draws differ between visits. AdamW is used with a learning rate of 10^{-4}, a weight decay of 10^{-4}, a 1,000-step warmup, cosine decay and gradient-norm clipping at 1, with bfloat16 autocast on CUDA. The checkpoint at step 1,505,000 minimised NLL on 32 fixed validation fields. This small selection subset contained no unconformity field, and the full validation and test splits remained separate.

Interpreting the training curve. Mean training and validation NLL declined from 1.010 and 1.072 between steps 100,000 and 200,000 to 0.830 and 0.826 over the final 220,000 steps. No validation field duplicated a training field; the closest training field to each validation field differed by RMSE 1.03–3.18 (median 1.59) $\log_{10} K$. Figure 3a averages 50 logged training losses per 5,000-step window. After step 1,200,000, sensor count explained 86% of the logged-loss variance; mean loss was 2.02 at $N = 4$ and -0.49 at $N = 4096$. Logging every 100 steps samples only 9 of the 36 scheduled conditions (all six counts at $\sigma \in \{0.05, 0.2, 1\}$). The training curve therefore cannot be interpreted as the validation NLL over all conditions.

Full-test evaluation. The selected checkpoint was evaluated once on 5,000 held-out fields at six sensor counts and 11 noise levels $\{0, 0.025, 0.05, 0.075, 0.1, 0.15, 0.2, 0.35, 0.5, 0.75, 1\}$ (66 conditions), with two independent noise draws per condition. For each field and count, one random layout is reused across noise levels and draws; within each draw, the same standardised

Gaussian noise is scaled by the chosen σ. At $N = 4096$, every cell is sensed; this setting therefore assesses denoising rather than interpolation.

C.2 Comparative and stress-test protocols

Paired benchmark. The comparison uses the first 100 test task IDs from each geological class (1,200 fields), selected without reference to scores. The equal class counts assign equal weight to each class. Selecting by task ID avoids any dependence on the scores, but because the subset is not a random sample, it is not guaranteed to be representative. The grid comprises six sensor counts and six noise levels $\sigma \in \{0, 0.05, 0.1, 0.2, 0.5, 1\}$ (36 conditions), with one noise draw per condition. Pooled scores from this benchmark and from the full test set are therefore reported separately.

Comparators. All methods receive identical fields, layouts and noise draws. GeoPFN and GeoPFN-V (Section B.4) receive the true σ. Kriging receives the sensor-noise variance and uses an anisotropic exponential covariance, a profiled constant mean and microscale variance. Its three variants use a global covariance prior, a class-specific prior supplied with the true class label (oracle), or per-field covariance fitting by regularised restricted maximum likelihood (REML) around the global parameters. Global and class-specific hyperparameters are fitted on clean training fields. At 4,096 sensors, per-field fitting uses 1,024 sensors, whereas prediction uses all sensors.

Three point predictors are scored by RMSE: inverse-distance weighting, nearest neighbour and natural neighbour. The natural-neighbour method uses the discrete Sibson scheme of Park et al. (2006) on the 64×64 grid. Each grid cell passes its nearest sensor's reading to every cell closer to it than that sensor; each cell then averages the readings it receives. The bounded grid defines predictions outside the sensors' convex hull, and sensed cells retain their readings.

Exceedance forecasts. The three thresholds are the 10th, 50th and 90th percentiles of clean training values, $Y_{10} = -8.87$, $Y_{50} = -5.53$ and $Y_{90} = -2.24$. The climatological reference forecasts the constant training exceedance probabilities 0.9, 0.5 and 0.1; its Brier score is evaluated against the test outcomes. Reliability plots bin forecast probabilities into ten groups.

Stress tests. Further paired suites vary the random layout (Appendix F.1), use structured layouts (Appendix F.2), replace independent Gaussian sensor errors with other error processes (Appendix G.1), supply incorrect or untrained noise levels and untrained sensor counts (Appendix G.2), and estimate an unknown σ from the sensors (Appendix H). All suites remain within the same synthetic generator and involve no retraining.

TabPFN-3.5 comparison. Table 4 and Figure 15 compare TabPFN-3.5 (Jäger et al., 2026) on the first ten fields of each class (120 fields), selected before scoring under all 36 conditions. All listed methods share fields, layouts and noise draws; we confirmed that the field identities and the scores of the other methods agree with a separate 120-field run. Each field is a separate regression task: normalised sensor coordinates are features, noisy readings are labels and the 4,096 query coordinates receive predictive distributions. Standard TabPFN-3.5 receives no noise input. The version with σ uses features x, y, $x^2 + \sigma x$ and $y^2 + \sigma y$ so that the noise level survives preprocessing that removes task-constant columns. These features do not specify a sensor-noise likelihood. Neither variant is fine-tuned.

Both variants ran locally with `tabpfn` 9.2.0, checkpoint `tabpfn-v3.5-20260909.safetensors`, eight estimators, random state zero and default GPU mixed precision. The timing protocol is described in Section I.2.

C.3 Metrics and uncertainty intervals

For clean target y_j, predictive mean m_j, predictive distribution function F_j and density p_j, the scores over J evaluated cells are

$$\begin{aligned} \mathrm{RMSE} &= \sqrt{\frac{1}{J}\sum_{j=1}^{J}(y_j - m_j)^2}, \qquad \mathrm{NLL} = -\frac{1}{J}\sum_{j=1}^{J}\log p_j(y_j), \\ \mathrm{CRPS} &= \frac{1}{J}\sum_{j=1}^{J}\int_{-\infty}^{\infty}[F_j(z) - \mathbf{1}\{y_j \le z\}]^2\,\mathrm{d}z. \end{aligned} \tag{C.1}$$

RMSE measures the error of the predictive mean, NLL penalises low density at the clean value, and CRPS compares the full predictive distribution with that value in the units of y; lower values are better for all three scores. NLL depends on the scale of the target and can be negative for a

concentrated density. Pooled RMSE is computed from pooled squared errors, not by averaging condition-level RMSEs; other pooled scores average cell-level contributions, and every condition contributes equally because all conditions have the same numbers of fields and cells.

The central $(1 - \alpha)$ interval is $[F_j^{-1}(\alpha/2), F_j^{-1}(1 - \alpha/2)]$. Coverage is the fraction of clean targets inside it, and width is the mean distance between its endpoints; coverage should equal the nominal level, and narrower intervals are preferable only at adequate coverage. The probability integral transform (PIT) value $u_j = F_j(y_j)$ is uniform for calibrated continuous marginals; a peak near 0.5 indicates excess spread, and excess mass near 0 and 1 indicates insufficient spread. A pooled PIT histogram can conceal subgroup miscalibration. In spread–skill plots, predicted spread is $\sqrt{\frac{1}{J}\sum_j V_j}$ and observed error is RMSE; their ratio (SSR) compares aggregate second moments, not full distributions.

For threshold t, the forecast exceedance probability is $p_j^{(t)} = 1 - F_j(t)$. The Brier score is $\frac{1}{J}\sum_j [p_j^{(t)} - \mathbf{1}\{y_j > t\}]^2$, and Brier skill $1 - \mathrm{BS}_{\mathrm{model}}/\mathrm{BS}_{\mathrm{clim}}$ is positive when the model has a lower squared probability error than climatology. Reliability diagrams compare the mean forecast probability with the observed event frequency in each probability bin. Material-boundary cells have a different material ID in at least one of their four neighbours; interior cells do not.

Reported confidence intervals resample whole fields within geological classes, keeping each field's conditions, layouts and noise draws together: 2,000 resamples for the full test set and 1,000 paired resamples for model differences. These intervals quantify variation across sampled fields, not across training seeds or independent sensor layouts.

Appendix D. Comparative scores and sensor density

Table D.1 pools the 36 paired conditions. Both GeoPFN variants have lower CRPS, NLL, 90% interval width and Y_{90} Brier score than all three kriging variants. GeoPFN-V improves on GeoPFN by 0.0026 in CRPS and 0.0084 in RMSE (paired 95% intervals 0.0021–0.0030 and 0.0072–0.0094), while GeoPFN is closer to nominal coverage and has slightly narrower intervals. The paired CRPS advantage of GeoPFN over per-field kriging is 0.0834–0.0894. Among point predictors, natural neighbour (RMSE 1.670) lies between inverse-distance weighting (1.628) and

nearest neighbour (1.917). It outperforms inverse-distance weighting at 64–1,024 sensors but not at 4 or 16, where many query cells lie outside the convex hull of the sensors.

Table D.1. Pooled scores on the 1,200-field paired benchmark across all 36 conditions. RMSE, CRPS and interval width are in $\log_{10} K$ *units, and Brier q90 is the Brier score for exceeding* Y_{90}*. ΔRMSE is the RMSE of each model minus that of GeoPFN, with its paired 95% confidence interval; positive values indicate a higher error than GeoPFN. Bold marks the best value in each column; for coverage, it marks the value closest to 0.90.*

Model	RMSE ↓	CRPS ↓	NLL ↓	Cov. 90	Width 90 ↓	Brier q90 ↓	ΔRMSE vs. GeoPFN (95% CI)
GeoPFN (this study)	1.499	0.591	0.768	**0.900**	**2.81**	**0.0452**	
GeoPFN-V	**1.491**	**0.588**	**0.755**	0.895	2.84	**0.0452**	−0.009 to −0.007
Kriging, global prior	1.529	0.710	1.214	0.905	4.29	0.0541	0.024 to 0.036
Kriging, class prior (oracle)	1.519	0.693	1.147	0.898	4.09	0.0536	0.014 to 0.026
Kriging, per-field REML	1.509	0.677	1.172	0.899	3.92	0.0516	0.003 to 0.016
Inverse-distance weighting	1.628	–	–	–	–	–	0.121 to 0.135

Model	RMSE ↓	CRPS ↓	NLL ↓	Cov. 90	Width 90 ↓	Brier q90 ↓	ΔRMSE vs. GeoPFN (95% CI)
Nearest neighbour	1.917	–	–	–	–	–	0.407 to 0.429
Natural neighbour	1.670	–	–	–	–	–	0.161 to 0.181

The pooled RMSE advantage over per-field kriging does not hold at every count (Table D.2, Figure D.1): kriging has the lowest RMSE at 64–1,024 sensors. At 1,024 sensors, its RMSE is 0.799 versus GeoPFN's 0.880; GeoPFN-V also has lower RMSE and CRPS than GeoPFN (0.836 and 0.255 versus 0.880 and 0.264). GeoPFN nevertheless retains a lower pooled RMSE and CRPS because its gains at the other counts outweigh these differences. Results at $N = 4096$ assess denoising, not sparse interpolation.

Table D.2. Paired-benchmark scores for each sensor count, pooled over the six noise levels. RMSE, CRPS and interval width are in $\log_{10} K$ *units. Bold marks the best value within each sensor count; for coverage, it marks the value closest to 0.90. These scores are not directly comparable with Figure 4, which uses the separate 5,000-field test set.*

Model	RMSE ↓	CRPS ↓	NLL ↓	Cov. 90	Width 90 ↓
***N* = 4**					
GeoPFN	2.198	**1.159**	**2.011**	0.878	5.84
GeoPFN-V	**2.195**	1.160	2.015	0.877	**5.80**
Kriging, global prior	2.318	1.278	2.250	0.885	7.28
Kriging, class prior (oracle)	2.318	1.263	2.211	0.878	7.14
Kriging, per-field REML	2.315	1.255	2.357	**0.887**	6.92
Inverse-distance weighting	2.431	–	–	–	–
Nearest neighbour	2.883	–	–	–	–

Model	RMSE ↓	CRPS ↓	NLL ↓	Cov. 90	Width 90 ↓
Natural neighbour	2.602	–	–	–	–
***N* = 16**					
GeoPFN	**1.929**	**0.924**	**1.646**	0.890	4.47
GeoPFN-V	1.930	0.926	1.652	0.889	**4.44**
Kriging, global prior	1.948	1.050	2.062	**0.899**	6.23
Kriging, class prior (oracle)	1.930	1.022	2.004	0.884	5.90
Kriging, per-field REML	1.933	1.011	2.233	0.880	5.60
Inverse-distance weighting	1.976	–	–	–	–
Nearest neighbour	2.418	–	–	–	–
Natural neighbour	2.074	–	–	–	–
***N* = 64**					
GeoPFN	1.603	0.674	1.184	0.898	**3.08**
GeoPFN-V	1.601	**0.673**	**1.183**	**0.899**	3.09
Kriging, global prior	1.599	0.826	1.831	0.904	5.11
Kriging, class prior (oracle)	1.575	0.799	1.744	0.892	4.77
Kriging, per-field REML	**1.567**	0.779	1.714	0.889	4.59
Inverse-distance weighting	1.651	–	–	–	–
Nearest neighbour	1.990	–	–	–	–
Natural neighbour	1.647	–	–	–	–
***N* = 256**					
GeoPFN	1.247	0.448	0.670	0.898	**1.90**
GeoPFN-V	1.224	**0.441**	**0.653**	0.902	2.03
Kriging, global prior	1.222	0.595	1.463	0.908	3.81
Kriging, class prior (oracle)	1.208	0.579	1.358	**0.901**	3.60
Kriging, per-field REML	**1.175**	0.553	1.283	0.903	3.47
Inverse-distance weighting	1.371	–	–	–	–
Nearest neighbour	1.555	–	–	–	–
Natural neighbour	1.283	–	–	–	–
***N* = 1,024**					
GeoPFN	0.880	0.264	0.068	0.906	**1.09**

Model	RMSE ↓	CRPS ↓	NLL ↓	Cov. 90	Width 90 ↓
GeoPFN-V	0.836	**0.255**	**0.044**	**0.903**	1.24
Kriging, global prior	0.841	0.380	0.755	0.915	2.51
Kriging, class prior (oracle)	0.842	0.372	0.664	0.913	2.42
Kriging, per-field REML	**0.799**	0.347	0.583	0.914	2.26
Inverse-distance weighting	1.120	–	–	–	–
Nearest neighbour	1.138	–	–	–	–
Natural neighbour	1.037	–	–	–	–
***N* = 4,096**					
GeoPFN	0.179	**0.075**	-0.972	0.929	0.48
GeoPFN-V	**0.178**	**0.075**	-1.019	**0.901**	**0.44**
Kriging, global prior	0.323	0.128	-1.076	0.920	0.77
Kriging, class prior (oracle)	0.310	0.123	-1.100	0.921	0.74
Kriging, per-field REML	0.297	0.118	**-1.136**	0.922	0.71
Inverse-distance weighting	0.466	–	–	–	–
Nearest neighbour	0.466	–	–	–	–
Natural neighbour	0.466	–	–	–	–

Calibration across probability levels. GeoPFN and GeoPFN-V tracked nominal coverage at every central interval level (50% intervals covered 48.4% and 47.5%), and their PIT histograms were nearly flat (Figure D.2). The kriging variants were conservative at central levels and approached nominal coverage only near 90%. For predicted standard deviations of about 0.05–3 $\log_{10} K$, observed RMSE broadly followed predicted spread for all probabilistic models. GeoPFN-V predicted standard deviations down to about 0.01 $\log_{10} K$, and below about 0.1 its observed RMSE slightly exceeded its predicted spread. Figure 15 repeats these diagnostics on the matched TabPFN set; there, the observed RMSE of TabPFN-3.5 exceeded its predicted standard deviation between about 0.06 and 1 $\log_{10} K$ and fell below it above about 1 $\log_{10} K$.

Exceedance forecasts. At the thresholds Y_{10}, Y_{50} and Y_{90} (Appendix C.2), the test exceedance frequencies were 0.90072, 0.49624 and 0.09676, giving climatological Brier scores of 0.08942,

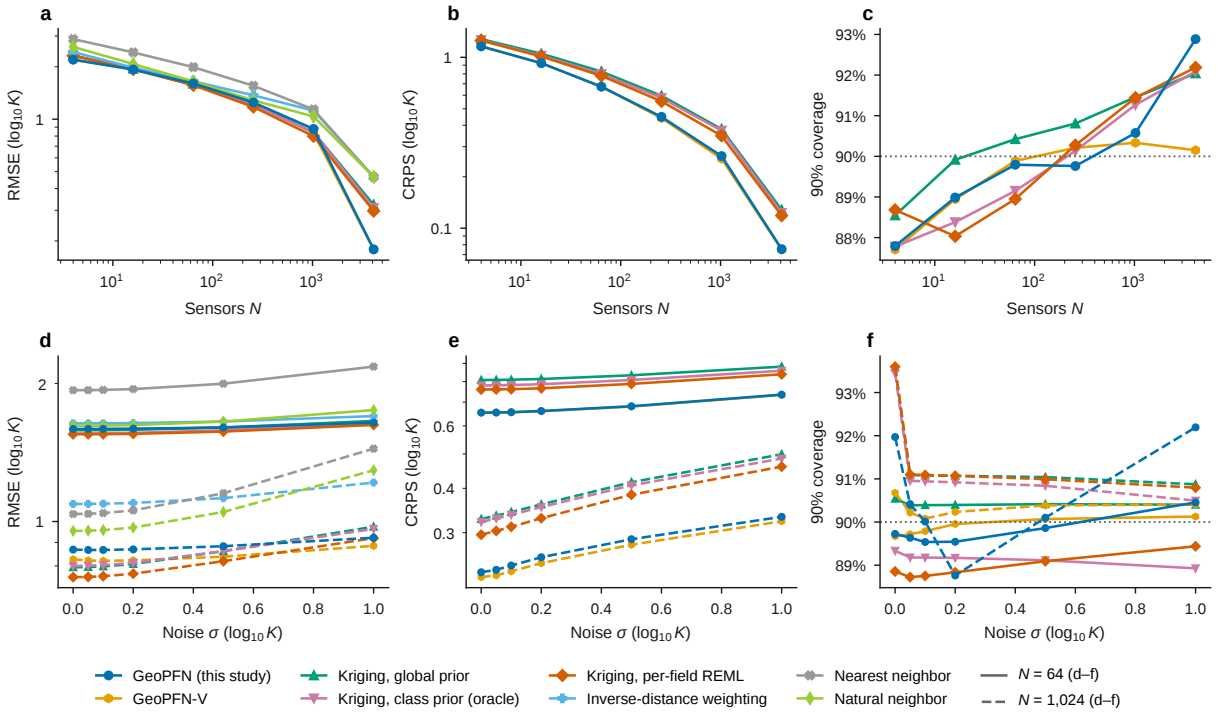


Figure D.1. Comparison of all models on the paired benchmark. The top row shows RMSE, CRPS and 90% coverage against sensor count, pooled over the six noise levels; the bottom row shows the same scores against noise level at $N = 64$ and 1,024. The dotted line marks the nominal 90% coverage. The neural models have the lowest CRPS at every sensor count, whereas per-field kriging has the lowest RMSE at 64–1,024 sensors.

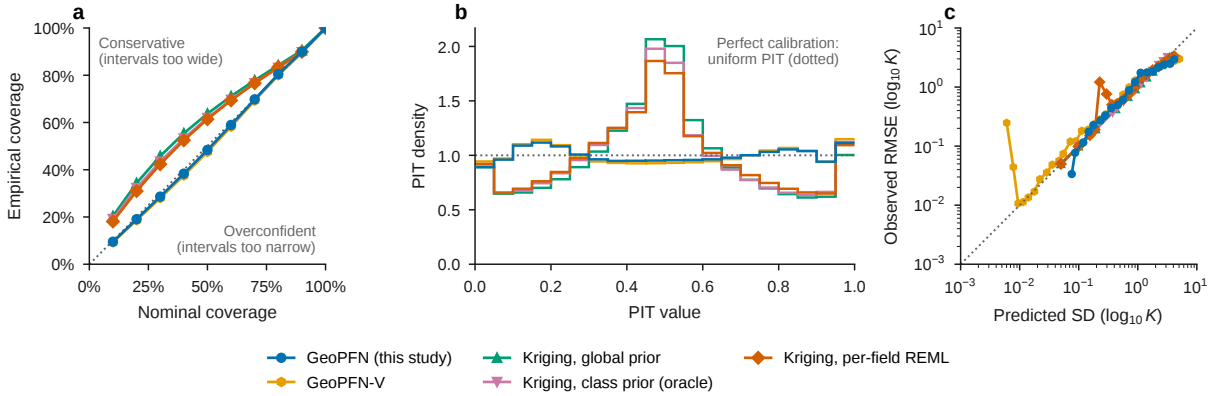


Figure D.2. Probabilistic calibration of the probabilistic models on the paired benchmark. (a) Observed coverage of central intervals against their nominal level; (b) PIT density; (c) observed RMSE against predicted standard deviation. Dotted lines mark ideal probabilistic calibration. Panel (c) omits kriging bins with RMSE below 10^{-6}, which come from noise-free sensor cells that kriging reproduces exactly. The curves pool spatially dependent cells and are therefore descriptive.

0.25000 and 0.08741. GeoPFN Brier scores were 0.03390, 0.11305 and 0.04523, and GeoPFN-V scores 0.03369, 0.11252 and 0.04517. The corresponding Brier skills were 0.621, 0.548 and 0.482 for GeoPFN, 0.623, 0.550 and 0.483 for GeoPFN-V and 0.478, 0.522 and 0.409 for per-field kriging; the two neural models differ considerably less from each other than from kriging or climatology. Reliability curves of the neural models lie close to the diagonal at the outer thresholds, whereas the kriging curves are steeper than the diagonal (Figure D.3). Plotted reliability bins contain at least 500 cell-condition observations, which is not a count of independent fields.

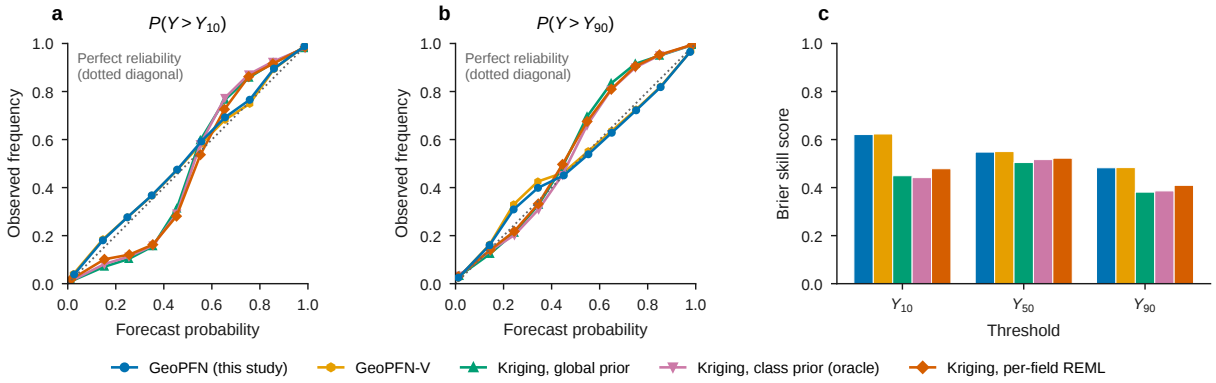


Figure D.3. Threshold-exceedance forecasts on the paired benchmark. Panels (a) and (b) show reliability diagrams for exceeding Y_{10} and Y_{90}, and panel (c) shows the Brier skill of each model relative to training climatology. Points close to the diagonal in (a) and (b) indicate that forecast probabilities match observed frequencies. The thresholds are defined in Section C.2.

Appendix E. Geological and spatial diagnostics

Full-test overview. Material boundaries showed the clearest calibration failure on the 5,000-field test set. They comprised 15.9% of evaluated cells, with RMSE 2.405 and 0.779 coverage for nominal 90% intervals, versus RMSE 1.268 and coverage 0.920 in interiors (Figure 5). Cells adjacent to sensors were covered less often than sensed cells (0.887 versus 0.928). Across classes, RMSE ranged from 0.979 for weathered bedrock to 2.059 for fracture networks; coverage ranged from 0.856 for cross-bedded fields to 0.914 for layers. These comparisons locate calibration failures but do not attribute them to a specific architectural component.

E.1 Boundaries and sensor status

Excluding fully sensed fields from the paired benchmark, GeoPFN covered 0.744 of unsensed boundary cells and 0.918 of unsensed interior cells; GeoPFN-V covered 0.774 of unsensed

boundary cells (Table E.1). Per-field kriging had lower boundary RMSE (2.439 versus 2.617 for GeoPFN) but lower coverage. Every model missed unsensed boundary targets in both tails (Table E.1; panel (c) of Figure E.1). The full-test boundary coverage of 0.779 differs from this value because it includes sensed cells, all six sensor counts, 11 noise levels, two draws and 5,000 fields.

Table E.1. Paired-benchmark scores for groups of cells defined by boundary and sensor status, excluding $N = 4096$. Boundary cells have at least one four-neighbour with a different material ID, and sensor status is assigned independently of boundary status. RMSE and CRPS are in $\log_{10} K$ units, and tail-miss rates are the percentages of targets below the 5% or above the 95% predictive quantile. For calibrated 90% intervals, coverage is 0.90 and each tail-miss rate is 5%; bold marks the value closest to these targets, or the lowest error, within each group.

Model	RMSE ↓	CRPS ↓	Cov. 90	Below q05	Above q95
Boundary					
GeoPFN	2.617	1.410	0.756	11.0	13.4
GeoPFN-V	2.581	1.385	**0.785**	**9.5**	**12.0**
Kriging, global prior	2.468	1.394	0.711	13.5	15.5
Kriging, class prior (oracle)	2.459	1.377	0.704	13.2	16.4
Kriging, per-field REML	**2.439**	**1.351**	0.705	13.4	16.2
Interior					
GeoPFN	1.382	**0.559**	0.920	3.5	4.6
GeoPFN-V	**1.381**	0.560	**0.915**	**3.7**	**4.8**
Kriging, global prior	1.471	0.719	0.938	2.9	3.3
Kriging, class prior (oracle)	1.460	0.700	0.929	3.1	4.0
Kriging, per-field REML	1.451	0.683	0.930	3.1	3.8
Sensor, boundary					
GeoPFN	**0.330**	**0.118**	**0.918**	**4.1**	**4.1**
GeoPFN-V	0.384	0.130	0.943	2.9	2.8
Kriging, global prior	0.532	0.202	0.861	7.1	6.8
Kriging, class prior (oracle)	0.503	0.194	0.861	7.0	6.8
Kriging, per-field REML	0.482	0.187	0.863	6.9	6.9
Sensor, interior					
GeoPFN	**0.210**	**0.089**	0.948	2.6	2.6
GeoPFN-V	0.213	**0.089**	0.932	**3.5**	3.3
Kriging, global prior	0.326	0.131	**0.929**	**3.5**	**3.6**
Kriging, class prior (oracle)	0.316	0.127	**0.929**	**3.5**	**3.6**

Model	RMSE ↓	CRPS ↓	Cov. 90	Below q05	Above q95
Kriging, per-field REML	0.308	0.124	0.930	**3.5**	3.5
Unsensed, boundary					
GeoPFN	2.707	1.502	0.744	11.5	14.1
GeoPFN-V	2.670	1.475	**0.774**	**10.0**	**12.7**
Kriging, global prior	2.551	1.480	0.700	13.9	16.1
Kriging, class prior (oracle)	2.542	1.462	0.692	13.7	17.1
Kriging, per-field REML	**2.521**	**1.435**	0.693	13.8	16.8
Unsensed, interior					
GeoPFN	**1.429**	**0.593**	0.918	3.5	4.7
GeoPFN-V	**1.429**	0.594	**0.913**	**3.7**	**4.9**
Kriging, global prior	1.520	0.761	0.939	2.8	3.3
Kriging, class prior (oracle)	1.508	0.741	0.929	3.1	4.0
Kriging, per-field REML	1.500	0.723	0.931	3.1	3.8

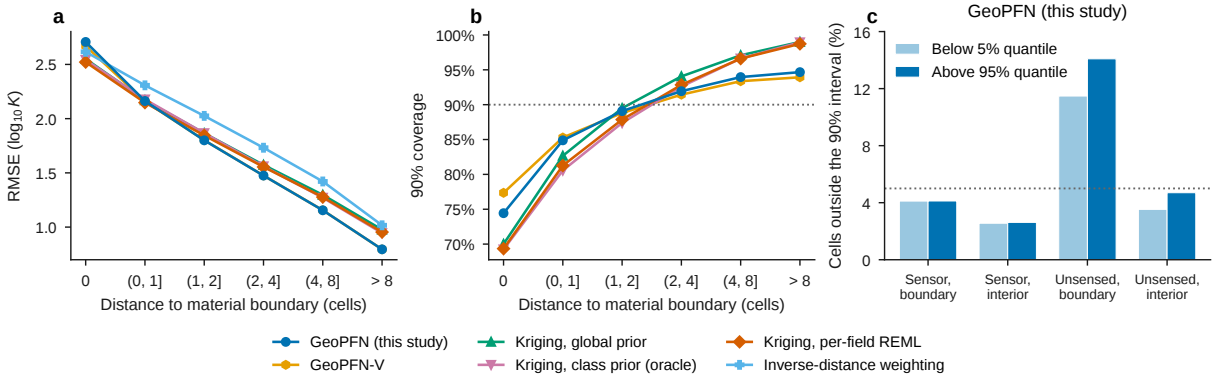


Figure E.1. Boundary diagnostics on the paired benchmark. (a) RMSE and (b) 90% coverage against distance to the nearest material boundary; (c) GeoPFN tail-miss rates by sensor and boundary status. Dotted lines mark the nominal 90% coverage and the nominal 5% per tail. Errors and undercoverage are concentrated at boundaries; tail misses alone, however, do not distinguish intervals that are too narrow from means that are biased.

E.2 Geological classes and materials

GeoPFN and GeoPFN-V class CRPS differed by at most 0.014 (fracture network); GeoPFN-V was lower in eight classes, GeoPFN in three, with one tie (Figure E.2). GeoPFN had lower CRPS than all kriging variants in every class, although cross-bedded fields remained undercovered.

Class-specific kriging reduced several coverage errors of global kriging. These classes represent mechanisms within a single generator rather than independent datasets.

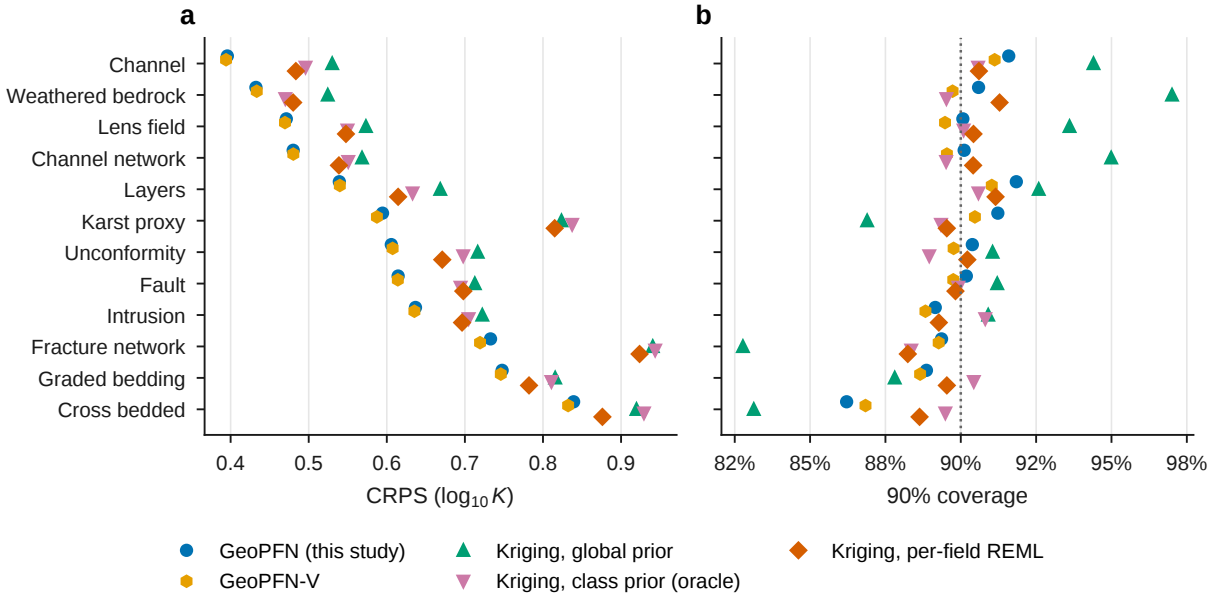


Figure E.2. CRPS and 90% coverage of each model for each synthetic geological class on the paired benchmark (100 fields per class). The dotted line marks the nominal 90% coverage. GeoPFN has lower CRPS than all kriging variants in every class, although some classes, most clearly cross-bedded fields, remain undercovered.

E.3 Qualitative reconstruction examples

Figure 12: field selection. The figure uses test IDs 96560 (layers), 95008 (channel), 98215 (lens field), 95007 (fault), 95054 (channel network) and 95011 (weathered bedrock). The classes were chosen for their contrasting structures, and no field was selected on the basis of reconstruction error. The layers field was selected visually for four steep, parallel layers among 42 finite test fields with four or five large layer regions and contacts crossing both grid directions. The lens field minimised the contrast between its most distinct lens and the background mean (1.73 $\log_{10} K$) among finite examples with at least 8% lens coverage. The channel network was selected visually for branching channels among the first 12 finite examples. The remaining three fields are the first finite test realisations of their classes.

Figure 12: common protocol. All six fields use the same 256 sensor locations on a regular 16×16 grid, $\sigma = 0.3$ and the same standardised Gaussian noise draw at each location (seed 20261136). Predictions used float32 on one CPU thread and the step-1,505,000 checkpoint.

Field RMSE is 0.596, 0.590, 0.434, 0.791, 0.950 and 0.434 in the order listed above. Clean, observed and predicted values use one colour scale; readings outside its range saturate. Each standard-deviation row has a separate scale starting at 0.01, so colours cannot be compared across components. Identical sensor geometry and noise input yield identical measurement maps. We verified that all outputs are finite, that each field has 256 unique sensor cells and that $V = S + M$ holds.

Figures 10 and 11. Both use test ID 95010, the first finite graded-bedding realisation, selected for its oblique contacts. Figure 11 places noise-free sensors at the centres of 2 × 2, 4 × 4, 8 × 8, 16 × 16 and 32 × 32 tiles, and at every cell; Figure 10 senses every cell at the six scheduled noise levels. The upper-left panel of each figure is the noise-free, fully sensed field and equals the clean target. Each layout uses a standardised Gaussian draw (seed 20261008 + N), scaled by σ. Boundary cells have a four-neighbour with a different material ID. We verified that the structural variance equals its floor at every sensed cell and that the measurement variance does not decrease between consecutive noise levels in Figure 10.

Figure 14: unseen-pattern protocol. Six synthetic patterns are generated directly at 256 × 256 cell centres. The 256 sensors form a regular 16 × 16 subset of the 64 × 64 grid of 4 × 4 fine-cell blocks; each reads the mean of its block. The locations are shared across fields. The unchanged checkpoint receives the negative of each rescaled I_c reading and is queried at all 65,536 fine-grid centres; the negated predictive mean is displayed. This test examines new shapes, numerical target rescaling and query resolution together; it does not assess calibration or transfer to measured I_c data.

Appendix F. Sensor-layout studies

F.1 Repeated random layouts

Five additional random layouts per field were evaluated alongside the main layout at 4–1,024 sensors and $\sigma \in \{0.1, 0.5\}$ (Figure F.1). Across the six layouts, GeoPFN's between-layout standard deviation was at most 0.0021 for coverage, 0.0069 for CRPS and 0.0107 for RMSE; the largest values occurred with 4 or 16 sensors. Per-field kriging varied similarly (at most 0.0030,

0.0110 and 0.0181). The main-grid results therefore varied little across the tested random layouts, although this does not establish similar stability under structured layouts (Section F.2).

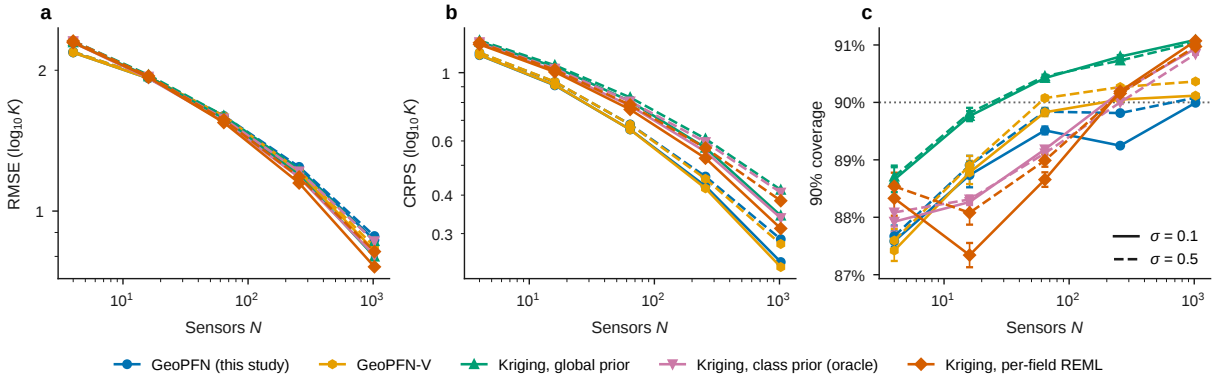


Figure F.1. Sensitivity of RMSE, CRPS and 90% coverage to the random sensor layout. Each field was evaluated with six random layouts at $\sigma = 0.1$ (solid lines) and 0.5 (dashed lines). Points show the mean, and error bars show one standard deviation between layouts; they do not represent training-seed uncertainty. The small error bars indicate that the main results depend little on the particular random layout.

F.2 Structured sensing

Regular grids, survey lines, sparse lines, four clusters and half-domain layouts were tested at $\sigma = 0.1$ and 0.5. Survey lines use all cells along evenly spaced rows; sparse lines sample every fourth cell along more rows at the same total sensor count. Clusters draw sensors around four centres, and half-domain layouts leave one half unsensed. Figure F.2 shows the results at $\sigma = 0.5$.

One of the two GeoPFN variants had the lowest CRPS at every tested layout and count. GeoPFN had lower CRPS than GeoPFN-V on survey lines up to 256 sensors and on all cluster and half-domain layouts; GeoPFN-V performed better on regular grids and sparse lines. GeoPFN had higher coverage on survey lines and clusters (0.858 versus 0.827 for 64 sensors on survey lines; 0.842 versus 0.816 for 256 clustered sensors). Nevertheless, its coverage fell to 0.842 with clusters and 0.870 on half-domain layouts, whereas global-prior kriging ranged from 0.889 to 0.912 across the tested layouts. Per-field kriging had lower RMSE with 256 clustered sensors (1.872 versus 1.956) and 512 half-domain sensors (1.560 versus 1.671). A lower CRPS therefore did not guarantee coverage near 0.90 for every sensor geometry.

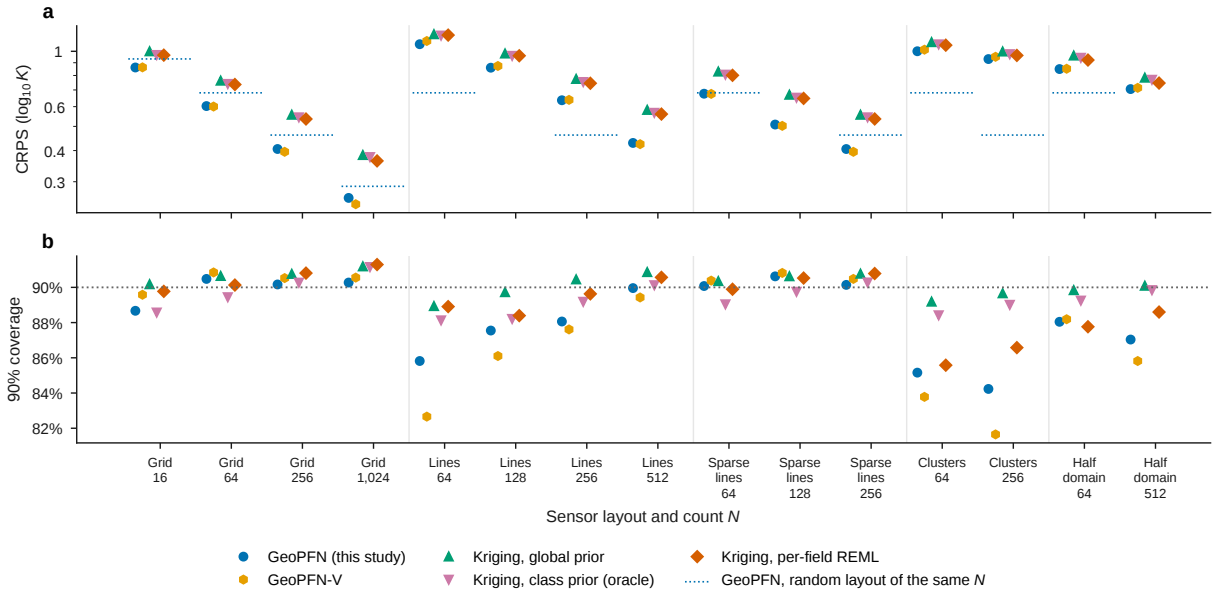


Figure F.2. Performance under structured sensor layouts at $\sigma = 0.5$: (a) CRPS and (b) 90% coverage for regular grids, survey lines, sparse lines, four clusters and half-domain layouts. Dotted markers show GeoPFN under a random layout with the same sensor count, where available. Coverage falls below nominal when large parts of the domain are unsensed.

Appendix G. Sensor-error processes and noise-input sensitivity

G.1 Changing the sensor-error process

The error-process suite uses 16, 256, 1,024 and 4,096 sensors at $\sigma = 0.2$ and 0.5. Alongside independent Gaussian errors, it tests variance-scaled Student-t_3 errors, a mixture with 5% fivefold-standard-deviation Gaussian outliers, and independent heteroscedastic errors whose sensor standard deviations are uniform on $[0, \sqrt{3}\sigma]$. The heteroscedastic input is their root-mean-square standard deviation. It also tests Gaussian errors smoothed over 3 or 10 grid cells and rescaled to marginal standard deviation σ, plus a common $+\sigma$ bias. None of the models is retrained. Figure G.1 shows the results at $\sigma = 0.5$.

Under the three independent non-Gaussian or heteroscedastic processes, GeoPFN's 90% coverage remained near nominal, between 0.889 and 0.927.

Spatial correlation and common bias caused larger deterioration as sensor density increased. Under 10-cell correlation, GeoPFN coverage fell from 0.877 at 16 sensors to 0.341 at 4,096; under common $+\sigma$ bias, it reached 0.283 at 4,096. GeoPFN-V exhibited even lower coverage under correlation (0.453 and 0.246 at 1,024 and 4,096 sensors, versus 0.509 and 0.341 for GeoPFN) and

under bias at 4,096 sensors (0.239). Global-prior kriging retained coverage of 0.800 and 0.679 in the two dense cases and lower CRPS under 10-cell correlation (0.309 versus 0.358). Denser sensing alone cannot remove an error that is shared across sensors. These synthetic tests reveal a limitation of the independent-error training assumption but do not validate an error model for a field site.

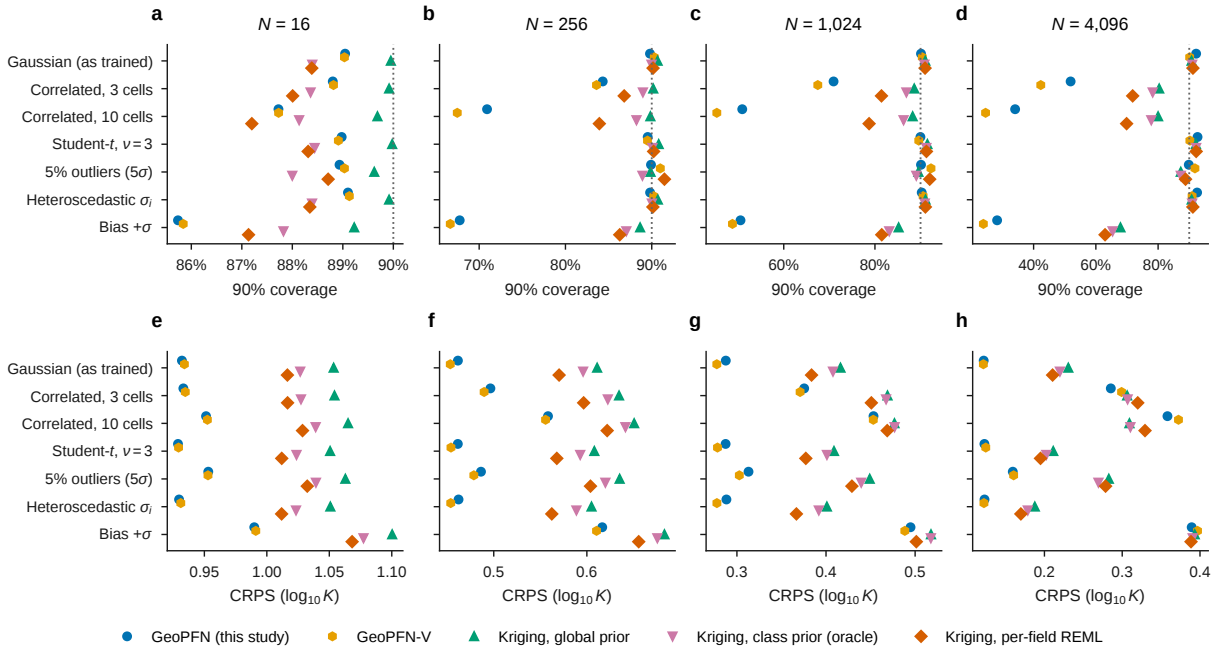


Figure G.1. Sensitivity to alternative sensor-error processes at $\sigma = 0.5$: 90% coverage (a–d) and CRPS (e–h) with 16, 256, 1,024 and 4,096 sensors. The dotted line marks the nominal 90% coverage. Independent non-Gaussian errors are tolerated, whereas spatially correlated errors and a common bias reduce coverage increasingly as sensors are added.

G.2 Supplied noise and untrained observation settings

Changing the supplied σ had a smaller effect with sparse than with fully observed grids. At $N = 4096$ and true $\sigma = 0.5$, supplying $\hat{\sigma} = 0$ gave 90% coverage of 0.075, while $\hat{\sigma} = 2\sigma$ gave 0.709. These are controlled changes to the input rather than evaluations of a noise estimator (Appendix H). For true $\sigma = 1.5$ or 2, beyond training, coverage was 0.891–0.933 over the six trained sensor counts. At five untrained counts, coverage was 0.883–0.915 except at $N = 2048$ with $\sigma = 0$ and 1, where it reached 0.952 and 0.930. Figure 8 presents these results; all fields are still drawn from the training generator.

Appendix H. Estimating unknown noise

The unknown-noise suite compares GeoPFN supplied with true σ against two estimates from the noisy observations, at $\sigma \in \{0.1, 0.2, 0.5, 1\}$ and $N \in \{64, 256, 1024, 4096\}$. The covariance method jointly fits spatial covariance and a free sensor-noise variance by per-field REML. The held-out method uses five sensor folds and selects the candidate σ maximising held-out predictive log density; the predictive variance for a held-out reading includes the candidate sensor-noise variance. Its candidate grid runs from 0 to 1.25, so an upper quantile at 1.25 signals grid saturation, not a precise estimate.

With 64–1,024 sensors, held-out estimates gave 90% coverage of 0.880–0.914 and covariance estimates 0.860–0.895 (Figure H.1). At 4,096 sensors, these ranges were 0.800–0.904 and 0.751–0.877. GeoPFN also undercovered at true $\sigma = 0.2$ and 4,096 sensors (0.853), so estimation error cannot account for all of the dense-grid miscalibration. At 64 sensors and true $\sigma = 1$, the covariance estimate had median 0.445 and the held-out estimates varied widely across fields. Near-nominal coverage with moderate sensor counts therefore does not imply accurate identification of σ.

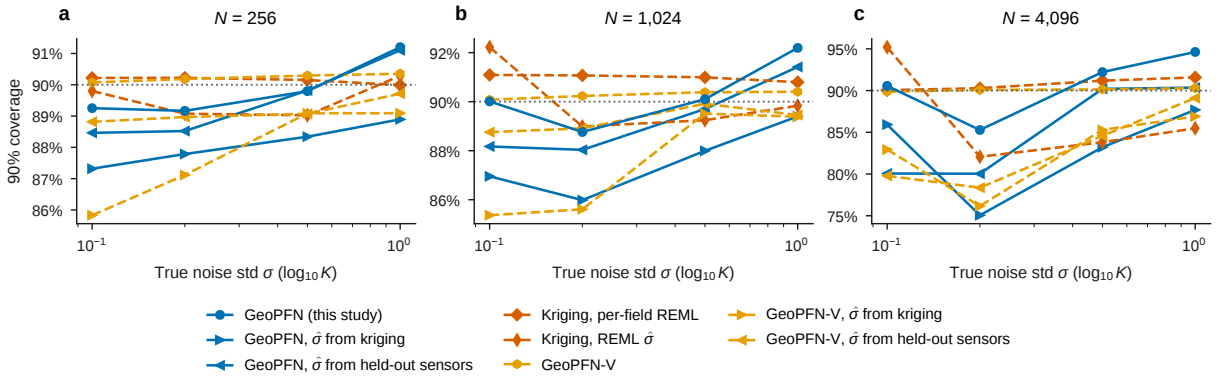


Figure H.1. 90% coverage of GeoPFN when the noise level is supplied exactly or estimated from the observations, at 256, 1,024 and 4,096 sensors. The dotted line marks the nominal coverage. Departures that also occur with the true σ cannot be attributed to noise estimation.

Appendix I. Computation and reproducibility

I.1 Per-field latency

Table I.1 reports GeoPFN latency on an Intel Xeon Platinum 8461V CPU (one numerical-library thread) and an NVIDIA RTX 6000 Ada GPU (48 GB). Both used float32 without autocast or TF32, evaluation mode, no gradients and 256-cell query chunks. For each device and sensor count, five warm-up calls preceded one timed forward pass on each of 1,000 distinct test fields (batch size one, 4,096 queries, $\sigma = 0.2$). Fields, layouts and noise draws were matched across devices. Timing used Python `perf_counter` with PyTorch 2.11.0 and CUDA 12.8 on 18 October 2026, synchronising the GPU around each call. Sensor embeddings and query features were recomputed; inputs and weights were already device-resident, so loading and transfer were excluded.

Table I.1. Distribution of GeoPFN latency per 4,096-cell field: median and 10th–90th percentiles over 1,000 fields for each setting. The percentiles describe variation across the timed fields; the corresponding means are given in Table 2.

Sensors	CPU median (ms)	CPU 10th–90th (ms)	GPU median (ms)	GPU 10th–90th (ms)
4	139.7	137.3–144.9	13.94	13.86–14.40
16	134.9	133.0–139.2	13.29	13.23–13.74
64	149.4	146.8–154.3	13.36	13.30–13.77
256	207.7	204.7–212.9	13.28	13.24–13.68
1,024	583.4	557.9–617.0	13.44	13.40–14.00
4,096	4,187.5	3,781.9–4,677.2	32.77	32.64–32.94

I.2 Same-session comparative timing

Table 4 reports local timing on one GPU, with each model timed on the first field of each class (12 fields), at $\sigma = 0.2$ and all six sensor counts. Batch size was one, TF32 was disabled, and five untimed warm-up calls preceded each count. GeoPFN, GeoPFN-V and kriging used float32 without autocast; TabPFN used its default GPU mixed precision, matching the scored predictions.

Each model was timed in a separate block and GPU calls were synchronised. A separate GPU process was observed at the end of the TabPFN timing run, so the measurements should not be read as isolated-hardware benchmarks.

GeoPFN and GeoPFN-V timing starts with inputs in CPU memory, includes encoding the 4,096 query coordinates and ends with CPU outputs. Caching query features changed GeoPFN times by less than 1 ms. Kriging starts with GPU-resident inputs; per-field REML includes 80 fitting steps. TabPFN timing includes synchronised fitting and prediction but excludes construction, checkpoint loading, transfers and scoring. Under TabPFN's default mixed precision, the means were 732 and 745 ms per field (rounded to 730 and 750 ms in Table 4), with fitting taking approximately 278 ms. Separate float32 TabPFN measurements took 1,681 and 1,725 ms; their predictions differed from the scored mixed-precision predictions by at most 0.016 $\log_{10} K$ RMS per field. The different transfer and precision conventions limit direct comparison of the elapsed times.

I.3 Computational cost

Sensor self-attention scales quadratically with sensor count, and decoder cross-attention scales with the product of query and sensor counts. Query chunking bounds decoder memory but not encoder cost. Training and periodic validation took 109.69 h of elapsed time, excluding data generation, tuning and evaluation. No deployment break-even point was estimated.

Appendix J. Limitations

Pooled coverage close to 0.90 concealed conditional failures (Table J.1). At unsensed boundaries, GeoPFN's coverage was 0.744, with misses in both tails (11.5% below the 5% quantile; 14.1% above the 95% quantile). Coverage also fell to 0.842 for four sensor clusters and 0.870 for half-domain sensing. The largest failures occurred with shared sensor error: at 4,096 sensors, coverage was 0.341 under 10-cell correlation and 0.283 under common $+\sigma$ bias, versus 0.800 and 0.679 for global-prior kriging. Estimating the noise level further reduced coverage in some dense-grid conditions (Appendix H). These failures restrict the use of the marginal intervals for site decisions unless they are validated for the intended geology, layout and error process. The protocols and full comparisons are given in Appendices E–H.

Table J.1. Coverage of nominal 90% intervals in selected stress conditions of the paired benchmark. Boundary results pool 4–1,024 sensors, and the layout and error-process rows use $\sigma = 0.5$. Values are proportions. The conditions were selected to summarise the main failures and do not form an exhaustive list.

Condition (N)	GeoPFN	GeoPFN-V	Global kriging	REML kriging
Unsensed boundary (4–1,024)	0.744	0.774	0.700	0.693
Four clusters (256)	0.842	0.816	0.897	0.866
Half domain (512)	0.870	0.858	0.901	0.886
Student-t_3 errors (1,024)	0.900	0.896	0.915	0.913
10-cell correlation (1,024)	0.509	0.453	0.883	0.787
10-cell correlation (4,096)	0.341	0.246	0.800	0.699
Common $+\sigma$ bias (4,096)	0.283	0.239	0.679	0.630